Examining the thermal properties of unirradiated nuclear grade graphite between 750 and 2500 K

T. R. Pavlov[1,2,3*], M. Lestak[2], M. R. Wenman[2], L. Vlahovic[1], D. Robba[1], A. Cambriani[1], D. Staicu, E. Dahms, M. Ernstberger[1], M. Brown[4], M. R. Bradford[4], R. J. M. Konings[1] and R. W. Grimes[2]

[1] *European Commission, Joint Research Centre (JRC) Karlsruhe P.O. Box 2340, 76125 Karlsruhe, Germany*

[2] *Department of Materials and Centre for Nuclear Engineering, Imperial College London, Royal School of Mines, London, SW7 2AZ, UK*

[3] *Idaho National Laboratory, Characterization and Advanced PIE Division, P.O. Box 1625, Idaho Falls, ID, 83415, USA*

[4] *EDF Energy Nuclear Generation Ltd, Barnett Way, Gloucester, GL4 3RS, UK*

Abstract

This study presents the first high temperature measurements (between 750 K and 2500 K) of thermal conductivity, thermal diffusivity, specific heat and spectral emissivity of virgin graphite samples (type IM1-24) from advanced gas-cooled reactor (AGR) fuel assembly bricks. Scanning electron microscope (SEM) and X-ray computed tomography (XRT) techniques were used to verify the presence of Gilsocarbon filler particles (a characteristic microstructural feature of IM1-24 graphite). All thermal properties were investigated in two orthogonal directions, which showed the effective macroscopic thermal conductivity to be the same (to within experimental error). This can be linked to the morphology of the filler particles that consist of concentrically aligned graphitic platelets. The resulting spherical symmetry allows for heat to flow in the same manner in both macroscopic directions. The current thermal conductivity results were compared to other isotropic grade graphite materials. The significant discrepancies between the thermal conductivities of the individual grades are likely the result of different manufacturing processes yielding variations in the microstructure of the final product. Differences were identified in the filler particle size and structure, and possibly the degree of graphitization compared to other reported nuclear graphites.

1. Introduction

Amongst its various applications, graphite is an important material in a number of current and future nuclear reactor designs. It simultaneously serves as: neutron moderator; neutron reflector; structural material guiding the flow of coolant, as well as the placement of fuel assemblies and instrumentation; and a heat sink in the event of power transients[1]. In particular, the 14 advanced gas-cooled reactors (AGRs), operating in the United Kingdom[2], utilise the material as a both a structural material and a

[*]Corresponding author. Tel: +1 208 533-7365. E-mail: tsvetoslav.pavlov@inl.gov (Tsvetoslav Pavlov)

neutron moderator[3]. In order to predict accurately the behaviour of nuclear grade graphite inside an AGR, the material's properties have to be well understood and accurately quantified.

Nuclear grade graphite has been studied widely, however its peculiar properties still pose a challenge to the scientific community. The material exhibits a hexagonal structure. Strong covalent bonds (σ-bonds) exist between carbon atoms in the basal plane; in contrast, the covalent bonds parallel to the prismatic planes are relatively weak (π-bonds)[4]. The hexagonal crystal structure and bonding lead to strong crystal anisotropy. This anisotropy translates into a directional dependence of thermal and electrical conductivity[5,6], elastic moduli[7] and thermal expansion[8]. Furthermore, the chosen route of fabrication will govern the evolution of texture in polycrystalline samples[7]. This could lead to a spectrum of possible property variations with respect to the measurement direction, temperature and other state variables.

Previous studies have investigated the thermal properties of various different grades of graphite. Engle and Kelly compared the dimensional changes under irradiation in fine grained, H-451 and pyrolytic graphite[9]. Kelly also reviewed the mechanisms (such as oxidation and radiation damage) via which irradiation can limit the lifetime of nuclear grade graphites[10] which have a direct impact on the thermo-physical properties of the material. Rasor and McClelland investigated four different types of graphite (3474 D, 7087, GBH, GBE) via an electrical heating method[11]. Based on their thermal expansion measurements, it was evident that a significant degree of anisotropy was present. Maruyama and Harayama measured the thermal conductivity of various nuclear graphite grades (IG 110, ETP 10, CX 2002U, GC 30) as a function of neutron radiation dose and temperature (300 to 1800 K)[2]. Marsden, measured the thermal conductivity of irradiated and unirradiated Gilsocarbon graphite in a single direction below 1000 K[12]. In these studies, however, no consideration was given to the possible directional dependence of thermal conductivity. A study performed by Taylor et al.[5] investigated the in-plane and out-of-plane thermal conductivities of three different graphite grades. One of these materials was Pile Grade A (PGA) graphite, which was used in gas-cooled Magnox reactors in the UK. They showed PGA graphite exhibits a strong degree of anisotropy. The current study will examine the thermal properties, and in particular thermal conductivity, of a different type of nuclear grade graphite (Gilsocarbon graphite type IM1-24). Un-irradiated samples were extracted from the reactor bricks of the Hartlepool and Dungeness AGR reactors. In this study measurements are performed for the first time on this type of nuclear grade graphite from 750 K to the very high temperature of 2500 K. These are performed in two orthogonal sample orientations to examine the degree of anisotropy of the material.

2. Methodology

2.1. Samples

Two virgin graphite billets were provided by EDF Energy from the Dungeness B and Hartlepool AGR production runs. The Dungeness samples were isotropic moulded grade 1 (IM1-24) graphite, manufactured by Anglo Great Lakes (AGL), while the Hartlepool specimens were Gilso Carbon Moulded B (GCMB) manufactured by British Acheson Electrodes Ltd (BAEL). The filler material is Gilsocarbon and for the binder a tar pitch was used. The material was first moulded to form a 'green bake' at ~1000°C and then graphitised using an Acheson furnace between 2100 and 3000°C. The graphitisation was performed under non-oxidising conditions by covering all billets with a thick, sacrificial layer of coke particles. The materials were, additionally, double impregnated with binder before graphitisation to increase the density. Finally, pellets were obtained by machining the final graphitised product (see Table 1 and Table 2 for specimen dimensions and relevant material properties).

It is important to note that the thermal conductivity measurements of the Hartlepool and Dungeness specimen were compared. The differences were within the uncertainty of the measurements. Thus, for the sake of conciseness and clarity, only the results obtained from the Dungeness specimen are presented in this work (please see Figure A1 in Appendix for a comparison between Hartlepool and Dungeness measurements).

2.2. Laser flash 1 / LAF 1 (750 K – 1750 K)

The set-up consists of a pulsed Nd:YAG laser (1064 nm), a high-temperature induction furnace that contains the specimen, and a radiation thermometer[13]. The absolute value of the temperature rise at the rear face of the specimen is measured by a calibrated fast response radiation thermometer with a temporal resolution of 0.1 ms. The surface temperature sensed by the radiation thermometer is corrected for the influence of the hot surrounding furnace (cavity effect). The laser beam has been characterized with respect to its spatial energy distribution. The absolute energy of the incident laser pulse is measured via a beam splitter, which reflects a part of the laser radiation (around 3%) towards a calibrated energy meter.

2.3. Continuous wave laser surface heating / CLASH (1700 K -2500 K)

The experiment is based on a high temperature laser flash set-up described in detail elsewhere[14–16]. Graphite samples are held by three zirconia pins, attached to a graphite sample holder. These are placed in a pressure vessel under an argon atmosphere at 3 bar. The transparent sapphire windows of the chamber allow for two continuous wavelength (Nd-YAG with λ = 1064 nm) lasers to preheat the front and rear side of the sample. Temperatures are continuously monitored via high speed pyrometers on each side of the sample. Once the sample has equilibrated at the target temperature, the front surface of the sample is exposed to a laser pulse of around 10 ms. Upon initiation of the laser pulse the pyrometers are triggered and the resulting temperature increase with respect to time is recorded on both the front and rear sides of the sample. The voltage readings are acquired via a general purpose

interface bus (GPIB) unit, which transfers the data to a personal computer. These data are then converted to radiance temperature readings. Using Wien's law and the measured spectral emissivity, radiance temperature is then converted to black-body temperature. Finally, a FFT (fast Fourier transform) filter is applied to the experimental data, in order to cut-off high frequency noise via a top hat low band pass filter[14].

A finite element (FE) model has been developed to describe the heat transfer conditions during the experiment and is described in previous work[14,16]. The model thermograms are fitted to experimental transients, with thermal conductivity, specific heat and total hemispherical emissivity as optimisation parameters.

Table 1. Summary of graphite sample characteristics and laser beam parameters.

Parameter (units)	**Values**
room temperature density ρ_{298} (kg m^{-3})	1780
sample porosity (%)	21.2
sample thickness (mm)	2
sample radius (mm)	4
beam spot radius (mm)	1.5
pulse duration (ms)	10

Table 2. Material properties of graphite used as input in the FE model.

Property	**Expression**	**Reference**
linear thermal expansion E(T) *	$1.08142\times10^{-9}T^2 + 3.70824\times10^{-6}T$	Hay[17]
density ρ(T)	$\rho_{298}\{1 + E\}^{-3}$	Hay[17]
$\varepsilon_{(1064\ nm)}$**	$4.053\times10^{-5}T + 0.874$	Hay[17]
$\varepsilon_{(645\ nm)}$**	$5.437\times10^{-5}T + 0.823$	this work

* fitted to reference experimental data.

** see equation 2.

2.4. Scanning electron microscopy (SEM) and X-ray computed tomography (XRT)

Scanning electron microscopy was performed via a Vega Tescan TS5130LSH microscope using a tungsten filament (200 V – 30 keV). Both secondary electrons and backscattered electrons were used for acquiring high resolution images.

X-ray computed tomography was acquired with a Nikon XTH 225 ST system equipped with a 225 kV µfocus X-ray source and a 16 bit flat panel detector. To generate a 3D volume a sequence of 2D X-ray images are collected while the sample is rotated 360 degrees between the X-ray source and the

detector. This sequence is then reconstructed by dedicated software in order to create a 3D data set composed of elementary units called voxel. Each voxel is associated with a grey level value which represents the extent of x-ray attenuation at the voxel location. These attenuation values depend on the density, atomic number and geometry of the specimen. The voxel size for the acquired 3D data set is approximately 12 µm. A 3x3 median filter was applied to reduce noise. An additional correction was carried out in order to minimize the beam hardening effect.

3. Results

In this section both experimental and theoretical results are presented and compared. Figure 1 provides a geometric representation Figure 1A shows a reactor brick with a hole from which a billet is extracted (see Figure 1B). The billet's z-axis is parallel to the radial direction of the brick. Two different measurement directions are investigated experimentally. These are referred to as parallel (∥) and perpendicular (⊥). The perpendicular (⊥) measurement direction is equivalent to the reactor brick's radial direction (see Figure 1D) while the parallel (∥) direction is representative of a random vector lying in the plane which is normal to the brick's radial direction (see Figure 1C).

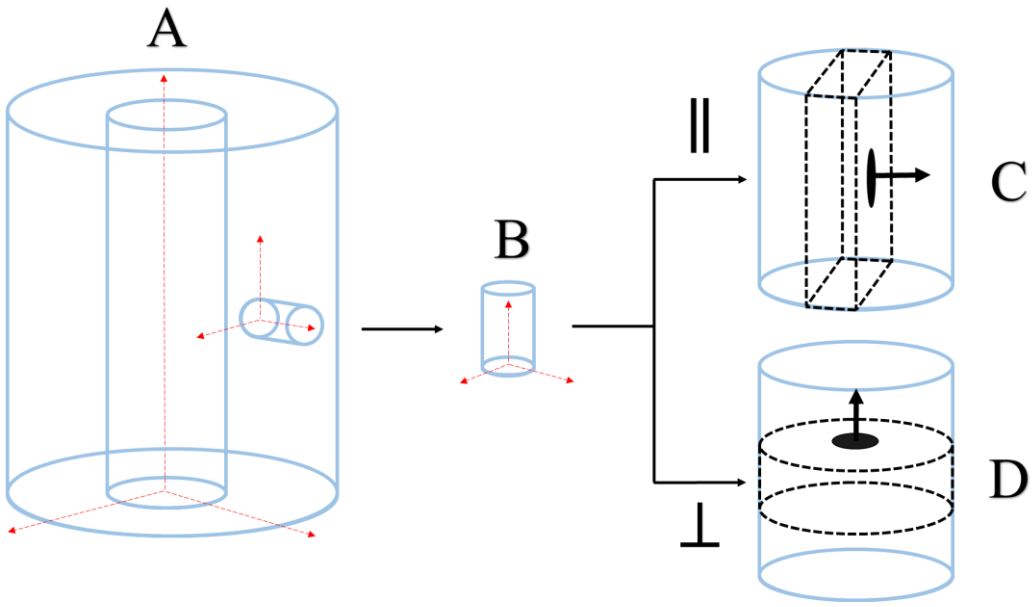

Figure 1 –Schematic of the geometries of the machined specimen and originating AGR brick. The red dotted arrows represent the axes of the various geometries. A) Schematic of an AGR brick from which a billet is machined; B) The machined billet rotated, such that its axial direction is equivalent to the brick's radial direction; C) Black dotted lines identify the edges of a cuboid machined from a cylindrical billet. The cuboid is representative of the parallel (∥) direction. The black arrow is normal to the measurement surface and parallel to direction of heat flow; D) Black dotted lines identify the edges of a cylinder (pellet) machined from a cylindrical billet. The pellet is representative of the perpendicular (⊥) direction. The black arrow is normal to the measurement surface and parallel to direction of heat flow.

3.1. Microstructure

Figure *2*A shows an SEM image of a cuboidal specimen machined from a Dungeness billet. The image shows the plane perpendicular to the normal drawn in Figure 1C (black arrow). Figure *2*B represents a zoom-in at a random location chosen from Figure *2*A. Figure *2*B shows the filler particles, binder matrix and microscale porosity. Figure 3 shows X-ray tomography images of a cylindrical specimen (see Figure 1D) machined from a Dungeness billet, such that its surface is perpendicular to the z-axis of the billet. The upper image in Figure 3 shows the horizontal cross-section of the sample while the lower image shows the vertical cross-section. The red dotted lines identify the cross-sectional areas of Gilsocarbon filler particles in both directions. Both Figure *2* and Figure 3 show the presence of lenticular microcracks, known as Mrozowski cracks, formed along basal planes during cooling from the graphitization process. These cracks extend tangentially to the spherical filler particles.

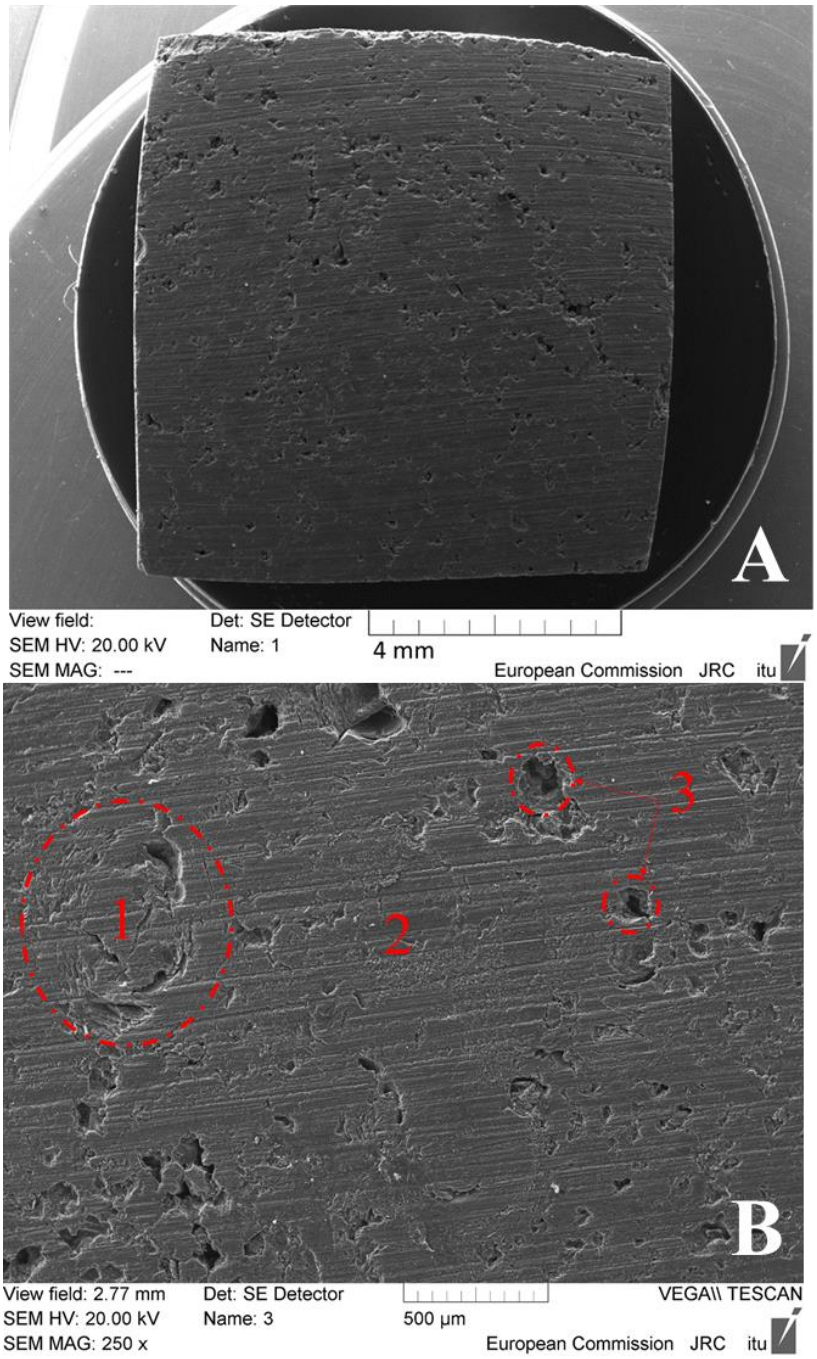

Figure 2- Secondary electron microscopy (SEM) images of the vertical cross-section of an IM1-24 graphite pellet. (A) Image shows the entire sample. (B) Image represents a zoom-in at a random location taken from the upper image. 1 - Gilsocarbon filler particle; 2 - Matrix composed of graphitised binder material; 3 - Pores of varying size and shape.

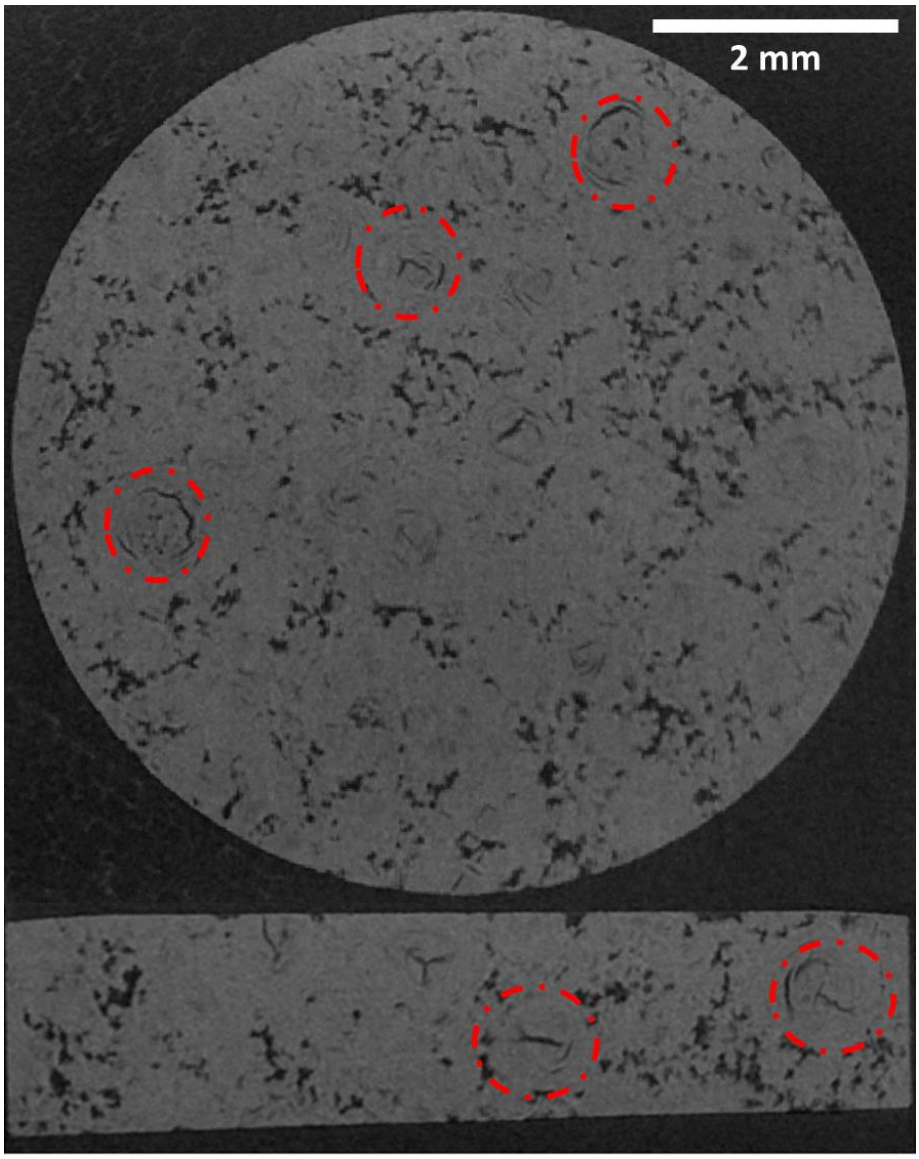

Figure 3 - X-Ray computed tomography images of an IM1-24 graphite pellet. The upper image represents the horizontal cross-section of the pellet while the lower image shows the vertical cross-section. The red dotted lines represent a few of the Gilsocarbon filler particles.

3.2. Thermal property measurements

In this section high-temperature measurements are presented for the following properties - spectral emissivity, thermal conductivity, specific heat and thermal diffusivity. The latter three properties have been plotted for two orthogonal directions. (Please refer to Tables A1 to A5 in the Appendix for the numerical values of the measurements.)

In Figure 4 spectral emissivity measurements are presented in the temperature range 1900 K and 2600 K. The linear fit of the data shows a marginal increase in emissivity from 0.92 at 1800 K to 0.96 at 2600 K. These results were used for the conversion of radiance temperature to black body temperature.

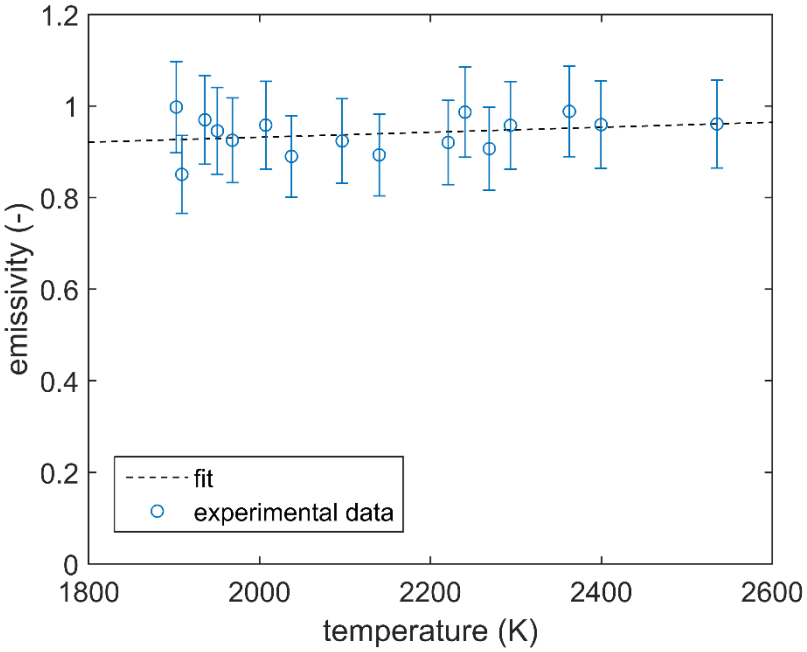

Figure 4 – Spectral emissivity at a laser wavelength of 645 nm as a function of temperature. The dotted line represents a linear fit, its coefficients are reported in Table 2.

Prior to examining the new experimental results of thermal conductivity, a function is proposed for the variation of thermal conductivity with temperature. Even though approximate, this model is based on the physical mechanisms responsible for the thermal transport in the material.

Graphite is a semi-metal, which means its Fermi level lies just above the conduction band. As a result, a minor portion of the electrons in the material are delocalised. These free charge carriers can contribute to properties such as electrical conductivity and thermal conductivity. Additionally, crystal vibrations also play a significant role in the evolution of thermal conductivity with temperature. Throughout this study, these two contributions are addressed as the electronic and lattice terms, respectively. Based on these mechanisms the following expression is used:

$$k_{tot} = k_l + k_{el} \quad (1)$$

where k_l is the lattice contribution and k_{el} is the electronic contribution. According to the Wiedmann-Franz law the electronic term can be expanded as follows:

$$k_{el}(T) = \sigma(T) L T \quad (2)$$

where σ is the electrical conductivity (S m^{-1}), L is the Lorentz number ($W\ \Omega\ K^{-2}$) and T is temperature (K). The Lorentz number recommended by Pavlov et al.[14] has been used ($L = 2.00 \times 10^{-8}\ W\ \Omega\ K^{-2}$). The electrical conductivity is approximated via an empirical function (see equation (3)). This function was deduced in a previous study[14] from the electrical resistivity data of Taylor and Groot[18]. It is important to note that this function is valid for temperatures above 1700 K[14]. This

simplification can be considered acceptable, since the electronic term is relatively small at lower temperatures.

$$\sigma(T) = \left(\frac{1}{2.15\times10^{-1}T + 5.56\times10^{2}}\right) \times 10^{8} \quad (3)$$

where the factor 10^8 is a unit conversion factor from $\mu\Omega^{-1}$ cm^{-1} to Ω^{-1} m^{-1}. (note: This factor was erroneously omitted in the study of Pavlov et al.[14], however it can be retrieved from the data presented by Taylor and Groot[18]). The lattice term is approximated via the following relationship:

$$k_l = \frac{1}{A+BT} \quad (4)$$

where A (W^{-1} m K) and B (W^{-1} m) are fitting constants, which have been obtained from the new experimental results (A = 5.08119×10^{-4} and B = 1.32025 ×10^{-5}). The overall fit is shown in Figure 5 and given by equation (5).

$$k_{tot} = \frac{2T}{2.15\times10^{-1}T + 5.56\times10^{2}} + \frac{1}{5.08119\times10^{-4}+1.32025\times10^{-5}T} \quad (5)$$

From Figure 5, it is evident that thermal conductivity decreases in the temperature range 500 K to 2500 K. Furthermore, Figure 5A shows that no significant differences were observed between the two orthogonal measurement directions. Figure 5B shows that the electronic contribution only becomes significant at higher temperatures (from ≈ 3% of k_{tot} at 1000 K to ≈ 14 % at 2500 K). Additionally, no variations in the properties were observed as a result of thermal cycling, although the laser flash measurements are relatively quick (of the order of seconds or minutes at most). Longer heating durations would be needed to be able to reach firm conclusions regarding thermal cycling.

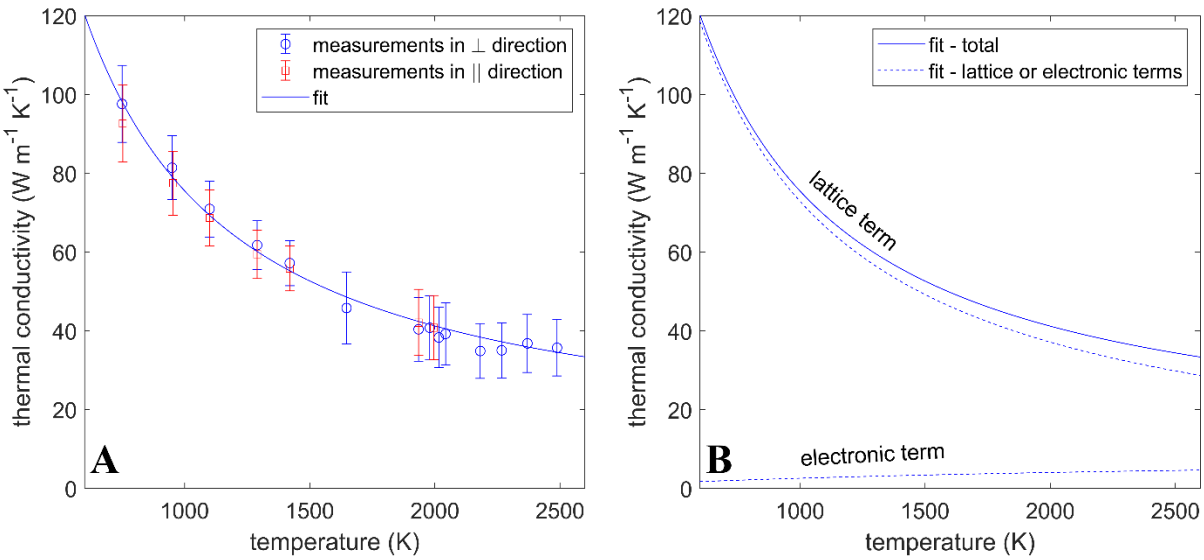

Figure 5 – Thermal conductivity of IM1-24 graphite as a function of temperature: (A) thermal conductivity measurements in two perpendicular directions alongside a fit to the data; (B) comparison of the fitted function and its constituent terms – electronic and lattice.

The measured specific heat values are shown in Figure 6. Within experimental error no differences are observed between the two measurement directions. While it is possible that specific heat may increase slightly in the temperature range 1600 K to 2500 K, within measurement uncertainty, this property can be considered invariant across this temperature range.

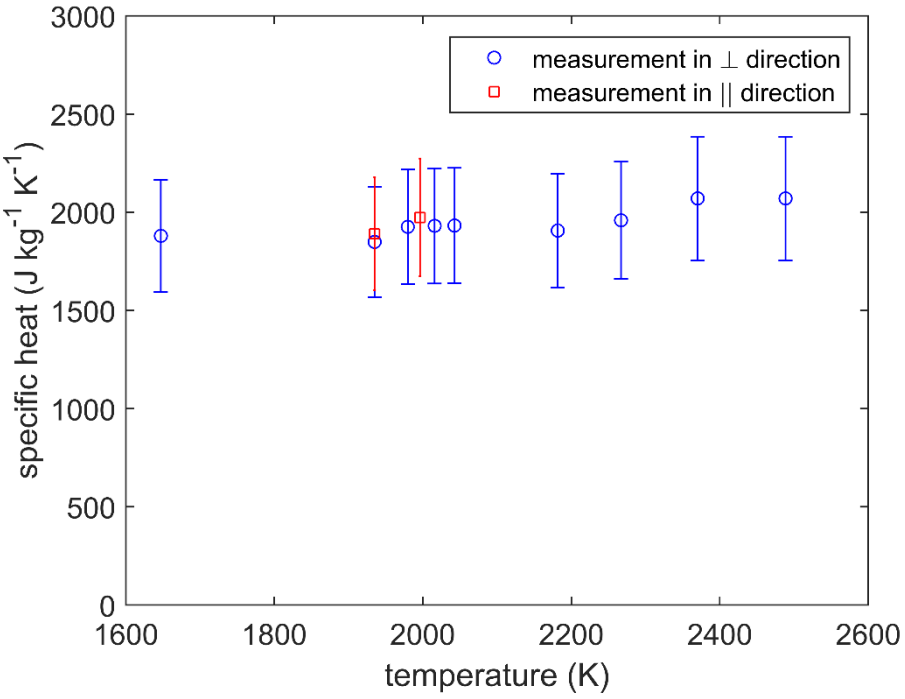

Figure 6 – Specific heat capacity as a function of temperature for two orthogonal directions.

Figure 7 shows the derived thermal diffusivity values as a function of temperature in the two different measurement directions. As for thermal conductivity, no directional dependence of the property was observed. The property decreases with respect to temperature from approximately $3.2 \times 10^{-5}\,m^2\,s^{-1}$ at 1000 K to $0.9 \times 10^{-5}\,m^2\,s^{-1}$ at 2500 K.

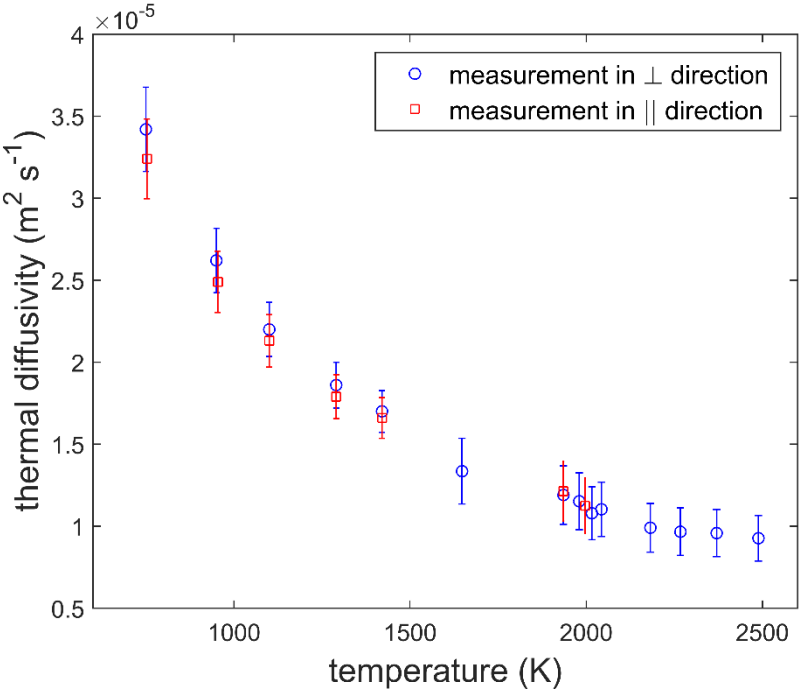

Figure 7 – Thermal diffusivity of IM1-24 graphite in two orthogonal directions.

3.3. Comparison of new results to available literature

In this section some of the newly measured results for nuclear graphite of type IM1-24 are compared to other grades of isotropic graphite – isostatically pressed and POCO AXM-5Q. Additionally, a solid state physics model is applied for comparison and to gain insight into the underlying physical processes.

Figure 8 demonstrates good agreement between the new results and the literature data on isostatically pressed graphite. The measurements performed on POCO graphite exhibit higher values, though still within the measurement uncertainty of the current results. The model proposed by Pavlov et al.[14] is in good agreement with all experimental data. It shows specific heat increases as a function of temperature up to 1000 K, from 0 $J\,kg^{-1}\,K^{-1}$ at 0 K, to 1800 $J\,kg^{-1}\,K^{-1}$ at 1000 K. At higher temperatures, the increase in specific heat with respect to temperature reduces and the curve flattens with only a relatively small increase observed between 2000 K and 2800 K.

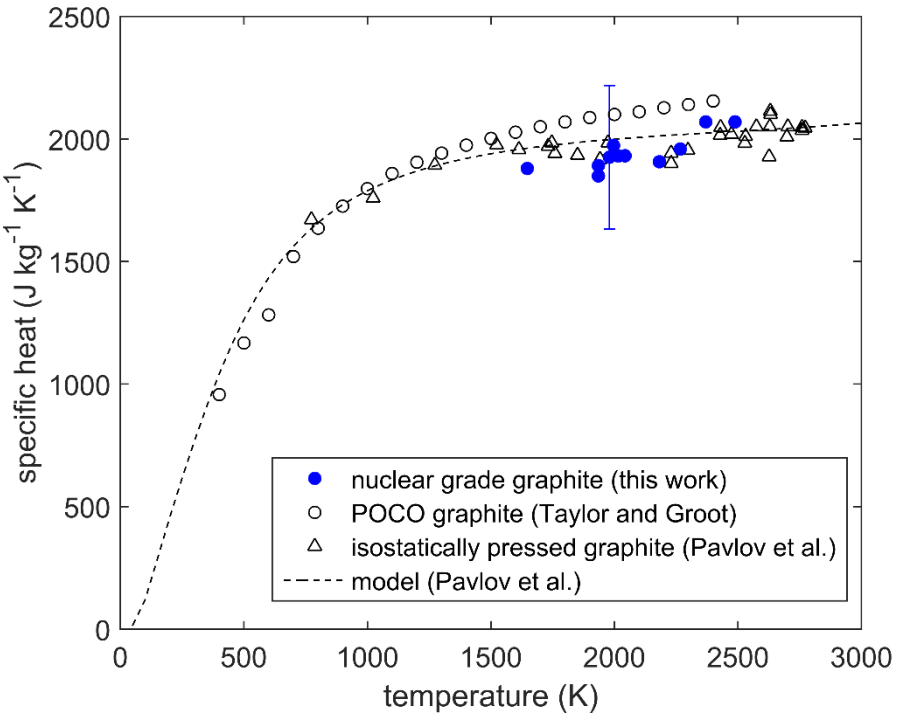

Figure 8 – Specific heat capacity as a function of temperature. The measurements performed in this work are compared to the experimental results of Taylor and Groot[18]*, Pavlov et al.*[14] *and assessed against the model proposed by Pavlov et al.* [14] *The blue error bar is indicative of a relative error of 20% on the current work's results (equivalent to two standard deviations).*

In Figure 9, the new measurements of thermal conductivity are compared to a nearly identical type of isotropic graphite measured by Taylor et al.[19] (Gilsocarbon A), as well as existing data sets on POCO graphite and isostatically pressed graphite. The lower temperature measurements in this study are in good agreement with the higher temperature measurements reported by Taylor et al.[19] The new results tend to be systematically higher compared to the POCO and isostatically pressed graphite albeit within the error bar at higher temperatures though not at lower temperatures. Isostatically pressed graphite exhibits the lowest values amongst the three material types. Furthermore, with increasing temperature the thermal conductivity differences between the graphite grades appear to decrease. All thermal conductivity values provide evidence for a systematic decrease in the value of the property in the examined temperature range (500 K to 2800 K). Furthermore, the model of Pavlov et al.[14] has been applied, in order to compare it to the new set of measurements. The model tends to capture correctly the decreasing trend of thermal conductivity. As previously shown by Pavlov et al.[14], the theoretical results agree with the experiments performed on isostatically pressed graphite.

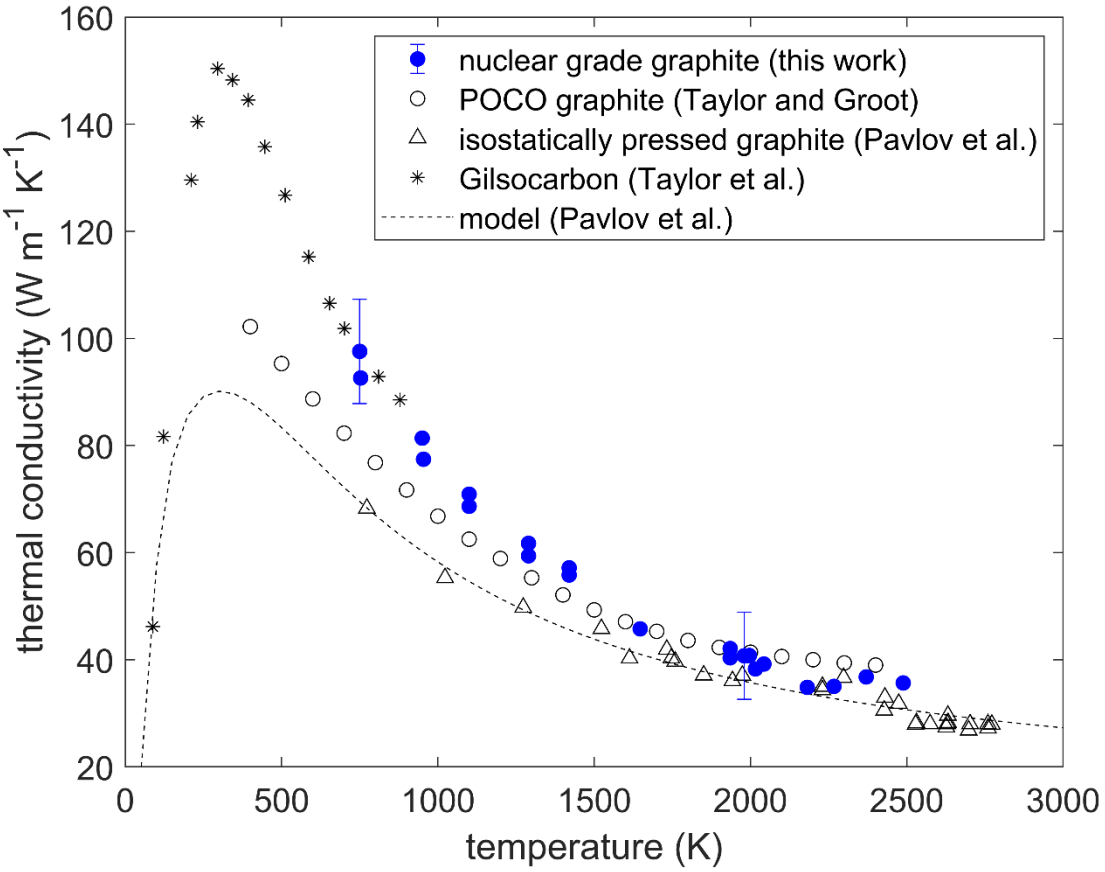

Figure 9 – Thermal conductivity as a function of temperature. The experimental data presented in this work is compared to the measurements of Taylor et al.[19], Taylor and Groot[18], Pavlov et al.[14] and the model proposed by Pavlov et al. [14]. The blue error bar is indicative of a relative error of 20% on the current work's results (equivalent to two standard deviations).

4. Discussion

4.1. Directional dependence of the thermal properties for IM1-24 type graphite

From the data presented in Figure 5 to Figure 7, it is clear that the properties of the AGR graphite are, to within experimental error, identical in two orthogonal directions over the studied temperature range. This is consistent with the reported isotropy in previous studies at lower temperatures[20]. The directional independence of thermal conductivity can be linked to the graphitic microstructure. In Figure 2 and Figure 3 the filler particles and graphitised binder matrix can be observed. The filler particles are characterised by lenticular pores and cracks along the particle circumference. These cracks have been characterised by Mrozowski[21–23]. They are parallel to the basal plane of the hexagonal crystal structure of graphite. These cracks derive from the difference in thermal expansion coefficients in the 'a' and 'c' directions of the hexagonal unit cell. The graphitic planes extending around the circumference of the filler spheres (along the Mrozowski cracks) impact the thermal conductivity tensor of these particles. The principal components of this tensor would be different in the radial and hoop directions, respectively. However, the existence of spherical symmetry means the particles do not exhibit a preferential orientation with respect to the direction of the heat flow. This is confirmed by the independence of thermal conductivity with respect to the direction of measurement. Furthermore, specific heat exhibits no directional dependence as it is a bulk (volumetric) property and is, therefore, scalar.

4.2. Comparing the new measurements to the open literature and condensed matter theory

Figure 8 shows the good agreement between the new measurements of specific heat capacity, previous work and the model. Specific heat increases up to 1000 K and then begins to saturate due to the absence of higher frequency phonon states. The relatively small linear ascent at temperatures above 2000 K is due to electronic contributions. A defect contribution would not be expected at temperatures below 3000 K as the formation energies of Frenkel pairs in graphite are very high (10.2 eV)[24].

Figure 9 compares the new measurements of the thermal conductivity of IM1-24 type graphite to other isotropic types of graphite. The Gilsocarbon measurements reported by Taylor et al. at around 750 K agree very well with the measurements performed on the Gilsocarbon graphite in this work. However, it is clear that significant differences exist between the three types of isotropic grades of graphite. Isostatically pressed graphite exhibits the lowest values of thermal conductivity at temperatures between approximately 750 K and 1500 K, followed by POCO AXM-5Q, with the new results on the

IM1-24 samples being the highest. At temperatures above 2000 K these differences appear to be smaller in magnitude. Possible reasons could include different impurity content, a possible degree of anisotropy in POCO graphite and isostatically pressed graphite or a different microstructure (e.g. different grain size distribution, porosity size and shape). It must be noted that a high purity content has been quoted for all these different materials[14,20,25] and hence it is unlikely for impurities to be the source of the observed differences. The thermal conductivities of POCO AXM-5Q and isostatically pressed graphite have been examined in different directions over a limited temperature range[25,26]. The reported results in these studies show isotropic behaviour of thermal conductivity[25,26]. Hence, anisotropy is probably not the reason for the observed discrepancies. This leads us to consider if it is the microstructure of these different materials that is leading to the thermal transport differences. In particular, that pore shape and size are having the most significant effect on the thermo-physical properties[27,28].

The nature of the filler material and fabrication process may have a significant impact on the material properties. During the fabrication of IM1-24 type graphite spherical Gilsocarbon particles are added as the filler material, while for POCO AXM-5Q graphite petroleum coke is used[29], and for isostatic graphite a combination of coke and graphite[30]. In the case of the IM1-24 type material, the presence of large filler particles with circumferentially wound graphitic platelets[31] may assist phonons to propagate along the basal plane of these sheets. Since the in-plane thermal transport is orders of magnitude higher, such a mechanism may provide an efficient path for thermal transport. In comparison, cold isostatically pressed samples do not consist of large filler particles, which is evident from the X-ray tomography results presented in Figure 10A and Figure 10B. This material exhibits crystallites in random orientations (see Figure 10E). Such an initial configuration could constrain the degree of graphitization[32–34] and inhibit the ability of heat to be transported via the strongly conductive basal planes. This could explain the superior thermal conductivity of IM1-24 compared to cold isostatically pressed graphite grades. POCO-AXM graphite contains 5 μm sized filler particles[35] in comparison to the 500 μm Gilsocarbon particles of the IM1-24 type material. A smaller particle size indicates a lower mean free path for phonons traveling along the particle's constituent graphene planes. Hence, it is understandable that POCO AXM specimen would exhibit a lower thermal conductivity compared to the IM1-24 samples.

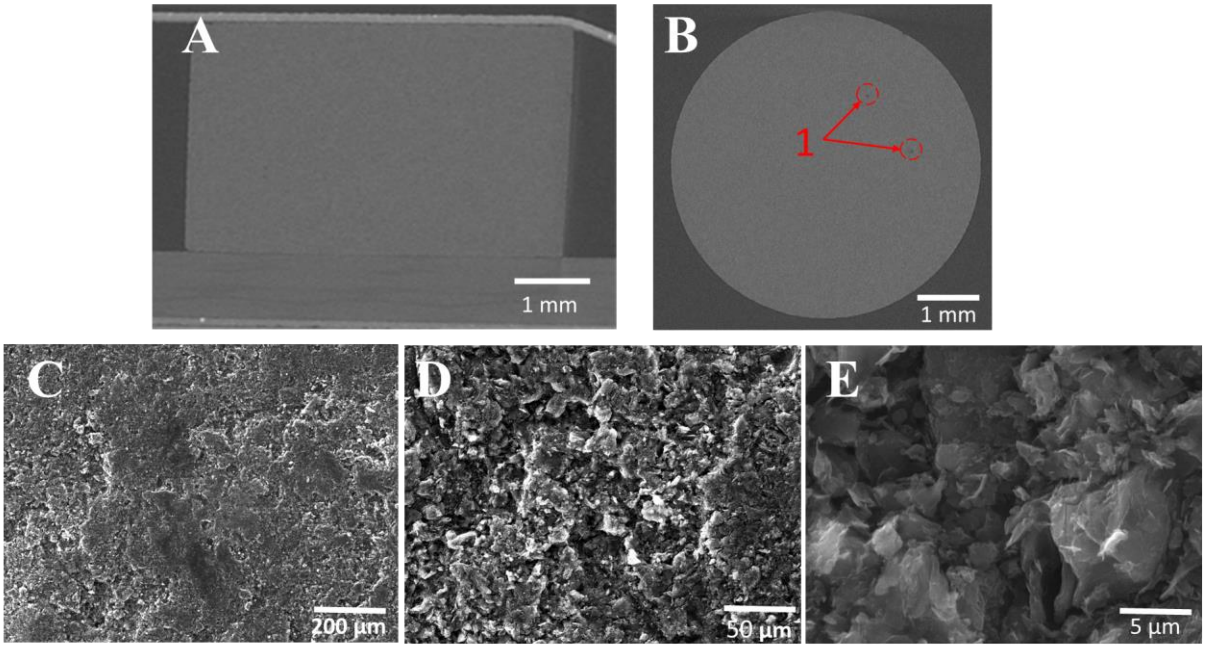

Figure 10 – Microstructural characterisation of isostatically pressed graphite pellets performed in this work the thermal conductivity of these specimen was examined in previous studies[14,15,17] (diameter: 5 mm / thickness: 3 mm / density: 1.81 g/cm^3). A) Vertical cross section of the sample measured via XRT; B) Horizontal cross section of the sample measured via XRT. The red circles associated with feature "1" mark microscopic pores with size comparable to the resolution limit of the device; C) SEM image of the sample showing surface porosity and a fine grain structure; D) SEM image (magnification of C) showing some partial grain structure; E) SEM image (magnification of D) showing randomly oriented lamellae.

In Figure 8 the prediction made using the solid state physics model of Pavlov et al.[14] is compared to the various experimental data sets from the different grades of isotropic graphite. The model assumes a homogeneous quasi-isotropic structure, which is not the case for IM1-24. However, randomly oriented lamellae are observed in fine grained isostatically pressed graphite (see Figure 10E), in accordance with the model assumption. Even though limited, the model does offer insight into certain physical mechanisms and their importance. The decrease in thermal conductivity as a function of temperature can be attributed predominantly to inelastic phonon-phonon interactions. Grain boundaries reduce the phonon mean free path only slightly and this reduction becomes less influential at higher temperatures. The interaction of phonons with electrons, as well as C^{13} impurities also leads to a minor reduction in thermal conductivity, which is most pronounced at near-ambient temperatures. Finally, it is clear that a multi-scale model would be needed to investigate all mechanisms for thermal transport at the different length scales.

5. Conclusions

- For the first time high temperature measurements (between 750 K and 2500 K) were performed to determine the thermal conductivity, thermal diffusivity, specific heat and spectral emissivity of unirradiated AGR graphite samples (type IM1-24) from Hartlepool and Dungeness power stations.

- All thermal properties were investigated in two orthogonal directions. The results showed the effective macroscopic thermal conductivity to be isotropic. This is consistent with the structure of the filler particles, which consist of concentrically aligned graphitic platelets.

- The solid state physics model for thermal conductivity is consistent with inelastic phonon scattering (lattice vibrations) dominating the high temperature behavior of graphite (above approximately 1000 K) followed by contributions from thermally mobilized electrons. However, the model does not capture the multi-scale nature of thermal transport in IM1-24 graphite.

Disclosure statement

Acknowledgements

The European Commission is acknowledged for the funding and experimental facilities provided to support the current work.

Appendix

Figure A1 compares the measured values of thermal conductivity obtained from specimen machined from the Dungeness and Hartlepool billets.

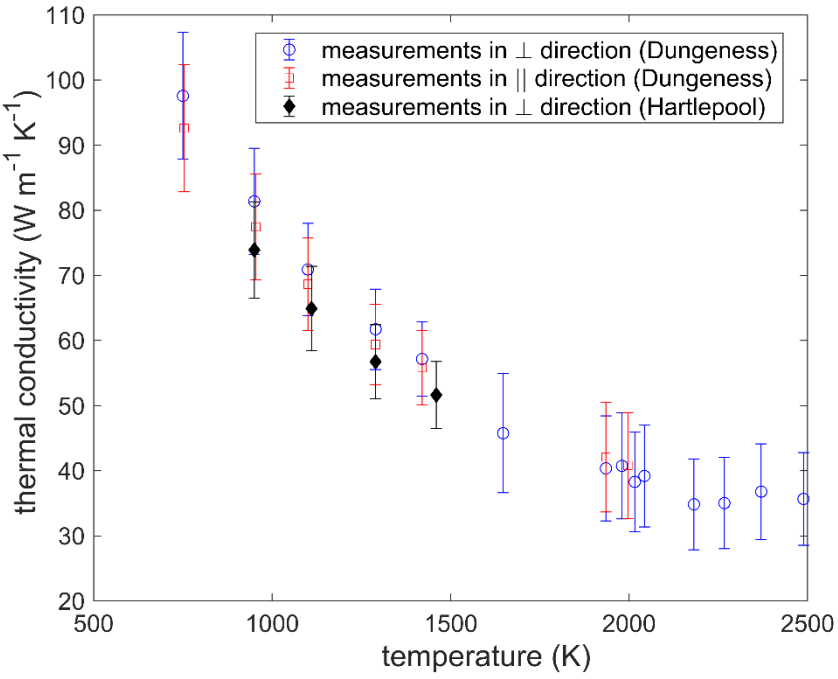

Figure A1 – Comparison between the thermal conductivity measurements obtained from the Dungeness and Hartlepool specimen as afunction of temperature

Tables A1 to A4 contain all measured values of thermal diffusivity, specific heat, thermal conductivity and spectral emissivity at 645 nm.

Table A1 – Measuremetns obtained in the perpendicular (⊥) direction via the Continuous wave Laser Surface Heating (CLASH) apparatus.

Temperature (K)	Thermal conductivity (W m^{-1} K^{-1})	Specific heat (J kg^{-1} K^{-1})	Thermal diffusivity (mm^2 s^{-1})
1980	40.7	1925.6	12.3
2370	36.8	2069.6	10.4
2488	35.7	2069.6	10.1
2016	38.3	1930.3	11.5
2267	35.0	1959.5	10.4
1647	45.8	1880.0	14.0
1935	40.36	1849.2	12.6
2043	39.19	1932.0	11.8
2182	34.84	1906.7	10.6

* thermal diffusivity is calculated via the equation $\alpha = \frac{k}{\rho \times c_P}$ (the correlations in Table 2 were used for the temperature dependent density)

Table A 2 Measuremetns obtained in the parallel (∥) direction via the Continuous wave Laser Surface Heating (CLASH) apparatus.

Temperature (K)	Thermal conductivity (W m^{-1} K^{-1})	Specific heat (J kg^{-1} K^{-1})	Thermal diffusivity * (mm^2 s^{-1})
1935	42.09	1891.4	12.9
1996	40.78	1973.3	12.0

* thermal diffusivity is calculated via the equation $\alpha = \frac{k}{\rho \times c_P}$ (the correlations in Table 2 were used for the temperature dependent density)

Table A3 - Measuremetns obtained in the parallel (⊥) direction via the Continuous wave Laser Surface Heating (CLASH) apparatus.

Temperature (K)	Thermal conductivity (W m^{-1} K^{-1})	Specific heat (J kg^{-1} K^{-1})	Thermal diffusivity (mm^2 s^{-1})
750	97.6	1613.5	34.2
950	81.4	1762.3	26.2
1100	70.9	1833.5	22.0
1290	61.7	1894.7	18.6
1420	57.2	1924.7	17.0

* thermal conductivity is calculated via the equation $k = \alpha \times \rho \times c_P$ (the correlations in Table 2 were used for the temperature dependent density)

** specific heat is calculated based on the validated model developed by Pavlov et al.[14]

Table A4 - Measuremetns obtained in the parallel (∥) direction via the Continuous wave Laser Surface Heating (CLASH) apparatus.

Temperature (K)	Thermal conductivity* (W m^{-1} K^{-1})	Specific heat** (J kg^{-1} K^{-1})	Thermal diffusivity (mm^2 s^{-1})
753	92.6	1616.4	32.4

954	77.4	1764.6	24.9
1100	68.6	1833.5	21.3
1290	59.4	1894.7	17.9
1420	55.8	1924.7	16.6

* thermal conductivity is calculated via the equation $k = \alpha \times \rho \times c_P$ (the correlations in Table 2 were used for the temperature dependent density)

** specific heat is calculated based on the validated model developed by Pavlov et al.[14]

Table A5 - Measured emissivity as a function of temperature.

Temperature (K)	Emissivity at 645 nm (-)
2362	0.99
2096	0.92
1936	0.97
1968	0.93
2007	0.96
2240	0.99
1903	1.00
2535	0.96
2400	0.96
1951	0.95
2269	0.91
2293	0.96
2037	0.89
2140	0.89
2221	0.92
1909	0.85

References

1. Marsden, B. J. Nuclear graphite for high temperature reactors. in *Gas turbine power conversion systems for modular HTGRs* 177–192 (2001). doi:10.1016/S1872-5805(17)60116-1

2. Maruyama, T. & Harayama, M. Neutron irradiation effect on the thermal conductivity and dimnesional change of graphite materials. *J. Nucl. Mater.* **195,** 44–50 (1992).

3. Nonbøl, E. *Description of the advanced gas cooled type of reactor (AGR)*. (Riso National Laboratory, NKS/RAK2(96)TR-C2, 1996).

4. Kelly, B. T. *The Physics of Graphite*. (Applied Science: London, 1981).

5. Taylor, R., Gilchrist, K. E. & Poston, L. J. Thermal conductivity of polycristalline graphite. *Carbon (1968)* **6,** 537–544 (1968).

6. Slack, G. A. Anisotropic thermal conductivity of pyrolitic graphite. *Phys. Rev.* **127,** 694–701 (1962).

7. Tsang, D. K. L. & Marsden, B. J. Constitutive material model for the prediction of stresses in irradiated anisotropic graphite components. *J. Nucl. Mater.* **381,** 129–136 (2008).

8. Marlowe, M. O. Elastic properties of three grades of fine grained graphite to 2000 C. 1–30 (1970).

9. Engle, G. B. & Kelly, B. T. Radiation damage of graphite in fission and fusion reactor systems. *J. Nucl. Mater.* **122,** 122–129 (1984).

10. Kelly, B. T. Graphite-the most fascinating nuclear material. *Carbon N. Y.* **20,** 3–11 (1982).

11. Rasor, N. S. & McClelland, J. D. Thermal properties of graphite, molybdenum and tantalum to their destruction temperatures. *J. Phys. Chem. Solids* **15,** 17–26 (1960).

12. Wen, K. Y., Marrow, T. J. & Marsden, B. J. The microstructure of nuclear graphite binders. *Carbon (2008)* **46,** 62–71 (2008).

13. Sheindlin, M., Halton, D., Musella, M. & Ronchi, C. Advances in the use of laser-flash techniques for thermal diffusivity measurement. *Rev. Sci. Instrum.* **69,** 1426–1436 (1998).

14. Pavlov, T., Vlahovic, L., Staicu, D., Konings, R. J. M., Wenman, M. R., Van Uffelen, P. & Grimes, R. W. A new numerical method and modified apparatus for the simultaneous evaluation of thermo-physical properties above 1500 K: A case study on isostatically pressed graphite. *Thermochim. Acta* **652,** (2017).

15. Pavlov, T. R., Staicu, D., Vlahovic, L., Konings, R. J. M., Van Uffelen, P. & Wenman, M. R. A new method for the characterization of temperature dependent thermo-physical properties.

Int. J. Therm. Sci. **124,** (2018).

16. Pavlov, T., Wenman, M. R., Vlahovic, L., Robba, D., Konings, R. J. M., Uffelen, P. Van & Grimes, R. W. Measurement and interpretation of the thermo-physical properties of UO_2 at high temperatures: the viral effect of oxygen defects. *Acta Mater.* **139,** 138–154 (2017).

17. Hay, B., Anhalt, K., Chapman, L., Boboridis, K., Hameury, J., Krenek, S., Vlahovic, L., Fleurence, N. & Beneš, O. Traceability improvement of high temperature thermal property measurements of materials for new fission reactors. *IEEE Trans. Nucl. Sci.* **61,** 2112–2119 (2014).

18. Taylor, R. E. & Groot, H. *Thermophysical Properties of POCO Graphite.* (Properties Research Lab, AFOSR-78-1375, 1978).

19. Taylor, R., Gilchrist, K. E. & Poston, L. J. Thermal conductivity of polycrystalline graphite. *Carbon (1968)* **6,** 537–544 (1968).

20. Middleton, P. M. & Moore, R. W. Role and development of nuclear graphite for gas cooled reactors, with particular reference to the high temperature reactor. in *International Nuclear Industries Fair* 1–15 (Nuclex 72, 1972).

21. Liu, D. & Cherns, D. Nano-cracks in a synthetic graphite composite for nuclear applications. *Philos. Mag.* **98,** 1272–1283 (2018).

22. Mrozowski, S. Mechanical strength, thermal expansion and structure of cokes and carbons. in *1st and 2nd Conferences on Carbon* 31 (1956).

23. Liu, D., Gludovatz, B., Barnard, H. S., Kuball, M. & Ritchie, R. O. Damage tolerance of nuclear graphite at elevated temperatures. *Nat. Commun.* **8,** 1–9 (2017).

24. Li, L., Reich, S. & Robertson, J. Defect energies of graphite: Density-functional calculations. *Phys. Rev. B - Condens. Matter Mater. Phys.* **72,** 1–10 (2005).

25. Sheppard, R. G., Mathes, D. M. & Bray, D. J. *Properties and characteristics of graphite for industrial applications*. (Poco Graphite Inc, 2001).

26. SGL carbon. *Specialty graphites for the photovoltaic industry*. (2015).

27. Ordonez-Miranda, J. & Alvarado-Gil, J. J. Effect of the pore shape on the thermal conductivity of porous media. *J. Mater. Sci.* **47,** 6733–6740 (2012).

28. Li, H., Zeng, Q. & Xu, S. Effect of pore shape on the thermal conductivity of partially saturated cement-based porous composites. *Cem. Concr. Compos.* **81,** 87–96 (2017).

29. Hust, J. G. *A fine-grained, isotropic graphite for use as NBS thermophysical property RM's*

from 5 to 2500 K. (1984). doi:10.15713/ins.mmj.3

30. Shen, K., Huang, Z. H., Hu, K., Shen, W., Yu, S., Yang, J., Yang, G. & Kang, F. Advantages of natural microcrystalline graphite filler over petroleum coke in isotropic graphite preparation. *Carbon N. Y.* **90,** 197–206 (2015).

31. Shen, K., Yu, S. & Kang, F. The microstructure and texture of Gilsocarbon graphite. *Carbon N. Y.* **153,** 428–437 (2019).

32. Oberlin, A. Carbonization and graphitization. *Carbon (1984)* **22,** 521–541 (1984).

33. Harris, P. J. F. Structure of non-graphitising carbons. *Int. Mater. Rev.* **42,** 206–218 (1997).

34. Rannou, I., Bayot, V. & M. Lelaurain. Structural charachterization of graphitization process in pyrocarbons. *Carbon (1994)* **32,** 833–843 (1994).

35. Woodcraft, A. L., Barucci, M., Hastings, P. R., Lolli, L., Martelli, V., Risegari, L. & Ventura, G. Thermal conductivity measurements of pitch-bonded graphites at millikelvin temperatures: Finding a replacement for AGOT graphite. *Cryogenics (Guildf).* **49,** 159–164 (2009).

Examining the thermal properties of unirradiated nuclear grade graphite between 750 and 2500 K

T. R. Pavlov[1,2,3*], M. Lestak[2], M. R. Wenman[2], L. Vlahovic[1], D. Robba[1], A. Cambriani[1], D. Staicu, E. Dahms, M. Ernstberger[1], M. Brown[4], M. R. Bradford[4], R. J. M. Konings[1] and R. W. Grimes[2]

[1] *European Commission, Joint Research Centre (JRC) Karlsruhe P.O. Box 2340, 76125 Karlsruhe, Germany*

[2] *Department of Materials and Centre for Nuclear Engineering, Imperial College London, Royal School of Mines, London, SW7 2AZ, UK*

[3] *Idaho National Laboratory, Characterization and Advanced PIE Division, P.O. Box 1625, Idaho Falls, ID, 83415, USA*

[4] *EDF Energy Nuclear Generation Ltd, Barnett Way, Gloucester, GL4 3RS, UK*

Abstract

This study presents the first high temperature measurements (between 750 K and 2500 K) of thermal conductivity, thermal diffusivity, specific heat and spectral emissivity of virgin graphite samples (type IM1-24) from advanced gas-cooled reactor (AGR) fuel assembly bricks. Scanning electron microscope (SEM) and X-ray computed tomography (XRT) techniques were used to verify the presence of Gilsocarbon filler particles (a characteristic microstructural feature of IM1-24 graphite). All thermal properties were investigated in two orthogonal directions, which showed the effective macroscopic thermal conductivity to be the same (to within experimental error). This can be linked to the morphology of the filler particles that consist of concentrically aligned graphitic platelets. The resulting spherical symmetry allows for heat to flow in the same manner in both macroscopic directions. The current thermal conductivity results were compared to other isotropic grade graphite materials. The significant discrepancies between the thermal conductivities of the individual grades are likely the result of different manufacturing processes yielding variations in the microstructure of the final product. Differences were identified in the filler particle size and structure, and possibly the degree of graphitization compared to other reported nuclear graphites.

1. Introduction

Amongst its various applications, graphite is an important material in a number of current and future nuclear reactor designs. It simultaneously serves as: neutron moderator; neutron reflector; structural material guiding the flow of coolant, as well as the placement of fuel assemblies and instrumentation; and a heat sink in the event of power transients[1]. In particular, the 14 advanced gas-cooled reactors (AGRs), operating in the United Kingdom[2], utilise the material as a both a structural material and a

*Corresponding author. Tel: +1 208 533-7365. E-mail: tsvetoslav.pavlov@inl.gov (Tsvetoslav Pavlov)

neutron moderator[3]. In order to predict accurately the behaviour of nuclear grade graphite inside an AGR, the material's properties have to be well understood and accurately quantified.

Nuclear grade graphite has been studied widely, however its peculiar properties still pose a challenge to the scientific community. The material exhibits a hexagonal structure. Strong covalent bonds (σ-bonds) exist between carbon atoms in the basal plane; in contrast, the covalent bonds parallel to the prismatic planes are relatively weak (π-bonds)[4]. The hexagonal crystal structure and bonding lead to strong crystal anisotropy. This anisotropy translates into a directional dependence of thermal and electrical conductivity[5,6], elastic moduli[7] and thermal expansion[8]. Furthermore, the chosen route of fabrication will govern the evolution of texture in polycrystalline samples[7]. This could lead to a spectrum of possible property variations with respect to the measurement direction, temperature and other state variables.

Previous studies have investigated the thermal properties of various different grades of graphite. Engle and Kelly compared the dimensional changes under irradiation in fine grained, H-451 and pyrolytic graphite[9]. Kelly also reviewed the mechanisms (such as oxidation and radiation damage) via which irradiation can limit the lifetime of nuclear grade graphites[10] which have a direct impact on the thermo-physical properties of the material. Rasor and McClelland investigated four different types of graphite (3474 D, 7087, GBH, GBE) via an electrical heating method[11]. Based on their thermal expansion measurements, it was evident that a significant degree of anisotropy was present. Maruyama and Harayama measured the thermal conductivity of various nuclear graphite grades (IG 110, ETP 10, CX 2002U, GC 30) as a function of neutron radiation dose and temperature (300 to 1800 K)[2]. Marsden, measured the thermal conductivity of irradiated and unirradiated Gilsocarbon graphite in a single direction below 1000 K[12]. In these studies, however, no consideration was given to the possible directional dependence of thermal conductivity. A study performed by Taylor et al.[5] investigated the in-plane and out-of-plane thermal conductivities of three different graphite grades. One of these materials was Pile Grade A (PGA) graphite, which was used in gas-cooled Magnox reactors in the UK. They showed PGA graphite exhibits a strong degree of anisotropy. The current study will examine the thermal properties, and in particular thermal conductivity, of a different type of nuclear grade graphite (Gilsocarbon graphite type IM1-24). Un-irradiated samples were extracted from the reactor bricks of the Hartlepool and Dungeness AGR reactors. In this study measurements are performed for the first time on this type of nuclear grade graphite from 750 K to the very high temperature of 2500 K. These are performed in two orthogonal sample orientations to examine the degree of anisotropy of the material.

2. Methodology

2.1. Samples

Two virgin graphite billets were provided by EDF Energy from the Dungeness B and Hartlepool AGR production runs. The Dungeness samples were isotropic moulded grade 1 (IM1-24) graphite, manufactured by Anglo Great Lakes (AGL), while the Hartlepool specimens were Gilso Carbon Moulded B (GCMB) manufactured by British Acheson Electrodes Ltd (BAEL). The filler material is Gilsocarbon and for the binder a tar pitch was used. The material was first moulded to form a 'green bake' at ~1000°C and then graphitised using an Acheson furnace between 2100 and 3000°C. The graphitisation was performed under non-oxidising conditions by covering all billets with a thick, sacrificial layer of coke particles. The materials were, additionally, double impregnated with binder before graphitisation to increase the density. Finally, pellets were obtained by machining the final graphitised product (see Table 1 and Table 2 for specimen dimensions and relevant material properties).

It is important to note that the thermal conductivity measurements of the Hartlepool and Dungeness specimen were compared. The differences were within the uncertainty of the measurements. Thus, for the sake of conciseness and clarity, only the results obtained from the Dungeness specimen are presented in this work (please see Figure A1 in Appendix for a comparison between Hartlepool and Dungeness measurements).

2.2. Laser flash 1 / LAF 1 (750 K – 1750 K)

The set-up consists of a pulsed Nd:YAG laser (1064 nm), a high-temperature induction furnace that contains the specimen, and a radiation thermometer[13]. The absolute value of the temperature rise at the rear face of the specimen is measured by a calibrated fast response radiation thermometer with a temporal resolution of 0.1 ms. The surface temperature sensed by the radiation thermometer is corrected for the influence of the hot surrounding furnace (cavity effect). The laser beam has been characterized with respect to its spatial energy distribution. The absolute energy of the incident laser pulse is measured via a beam splitter, which reflects a part of the laser radiation (around 3%) towards a calibrated energy meter.

2.3. Continuous wave laser surface heating / CLASH (1700 K -2500 K)

The experiment is based on a high temperature laser flash set-up described in detail elsewhere[14–16]. Graphite samples are held by three zirconia pins, attached to a graphite sample holder. These are placed in a pressure vessel under an argon atmosphere at 3 bar. The transparent sapphire windows of the chamber allow for two continuous wavelength (Nd-YAG with λ = 1064 nm) lasers to preheat the front and rear side of the sample. Temperatures are continuously monitored via high speed pyrometers on each side of the sample. Once the sample has equilibrated at the target temperature, the front surface of the sample is exposed to a laser pulse of around 10 ms. Upon initiation of the laser pulse the pyrometers are triggered and the resulting temperature increase with respect to time is recorded on both the front and rear sides of the sample. The voltage readings are acquired via a general purpose

interface bus (GPIB) unit, which transfers the data to a personal computer. These data are then converted to radiance temperature readings. Using Wien's law and the measured spectral emissivity, radiance temperature is then converted to black-body temperature. Finally, a FFT (fast Fourier transform) filter is applied to the experimental data, in order to cut-off high frequency noise via a top hat low band pass filter[14].

A finite element (FE) model has been developed to describe the heat transfer conditions during the experiment and is described in previous work[14,16]. The model thermograms are fitted to experimental transients, with thermal conductivity, specific heat and total hemispherical emissivity as optimisation parameters.

Table 1. Summary of graphite sample characteristics and laser beam parameters.

Parameter (units)	Values
room temperature density ρ_{298} (kg m^{-3})	1780
sample porosity (%)	21.2
sample thickness (mm)	2
sample radius (mm)	4
beam spot radius (mm)	1.5
pulse duration (ms)	10

Table 2. Material properties of graphite used as input in the FE model.

Property	Expression	Reference
linear thermal expansion E(T) *	$1.08142\times10^{-9}T^2 + 3.70824\times10^{-6}T$	Hay[17]
density ρ(T)	$\rho_{298}\{1 + E\}^{-3}$	Hay[17]
$\varepsilon_{(1064\ nm)}$**	$4.053\times10^{-5}T + 0.874$	Hay[17]
$\varepsilon_{(645\ nm)}$**	$5.437\times10^{-5}T + 0.823$	this work

* fitted to reference experimental data.

** see equation 2.

2.4. Scanning electron microscopy (SEM) and X-ray computed tomography (XRT)

Scanning electron microscopy was performed via a Vega Tescan TS5130LSH microscope using a tungsten filament (200 V – 30 keV). Both secondary electrons and backscattered electrons were used for acquiring high resolution images.

X-ray computed tomography was acquired with a Nikon XTH 225 ST system equipped with a 225 kV µfocus X-ray source and a 16 bit flat panel detector. To generate a 3D volume a sequence of 2D X-ray images are collected while the sample is rotated 360 degrees between the X-ray source and the

detector. This sequence is then reconstructed by dedicated software in order to create a 3D data set composed of elementary units called voxel. Each voxel is associated with a grey level value which represents the extent of x-ray attenuation at the voxel location. These attenuation values depend on the density, atomic number and geometry of the specimen. The voxel size for the acquired 3D data set is approximately 12 µm. A 3x3 median filter was applied to reduce noise. An additional correction was carried out in order to minimize the beam hardening effect.

3. Results

In this section both experimental and theoretical results are presented and compared. Figure 1 provides a geometric representation Figure 1A shows a reactor brick with a hole from which a billet is extracted (see Figure 1B). The billet's z-axis is parallel to the radial direction of the brick. Two different measurement directions are investigated experimentally. These are referred to as parallel (∥) and perpendicular (⊥). The perpendicular (⊥) measurement direction is equivalent to the reactor brick's radial direction (see Figure 1D) while the parallel (∥) direction is representative of a random vector lying in the plane which is normal to the brick's radial direction (see Figure 1C).

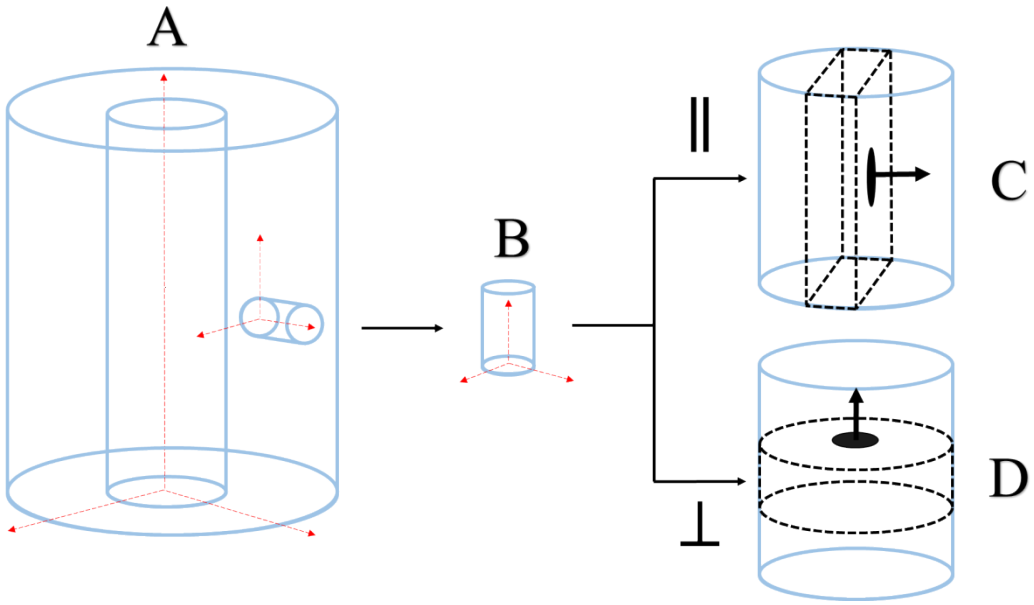

Figure 1 –Schematic of the geometries of the machined specimen and originating AGR brick. The red dotted arrows represent the axes of the various geometries. A) Schematic of an AGR brick from which a billet is machined; B) The machined billet rotated, such that its axial direction is equivalent to the brick's radial direction; C) Black dotted lines identify the edges of a cuboid machined from a cylindrical billet. The cuboid is representative of the parallel (∥) direction. The black arrow is normal to the measurement surface and parallel to direction of heat flow; D) Black dotted lines identify the edges of a cylinder (pellet) machined from a cylindrical billet. The pellet is representative of the perpendicular (⊥) direction. The black arrow is normal to the measurement surface and parallel to direction of heat flow.

3.1. Microstructure

Figure 2A shows an SEM image of a cuboidal specimen machined from a Dungeness billet. The image shows the plane perpendicular to the normal drawn in Figure 1C (black arrow). Figure 2B represents a zoom-in at a random location chosen from Figure 2A. Figure 2B shows the filler particles, binder matrix and microscale porosity. Figure 3 shows X-ray tomography images of a cylindrical specimen (see Figure 1D) machined from a Dungeness billet, such that its surface is perpendicular to the z-axis of the billet. The upper image in Figure 3 shows the horizontal cross-section of the sample while the lower image shows the vertical cross-section. The red dotted lines identify the cross-sectional areas of Gilsocarbon filler particles in both directions. Both Figure 2 and Figure 3 show the presence of lenticular microcracks, known as Mrozowski cracks, formed along basal planes during cooling from the graphitization process. These cracks extend tangentially to the spherical filler particles.

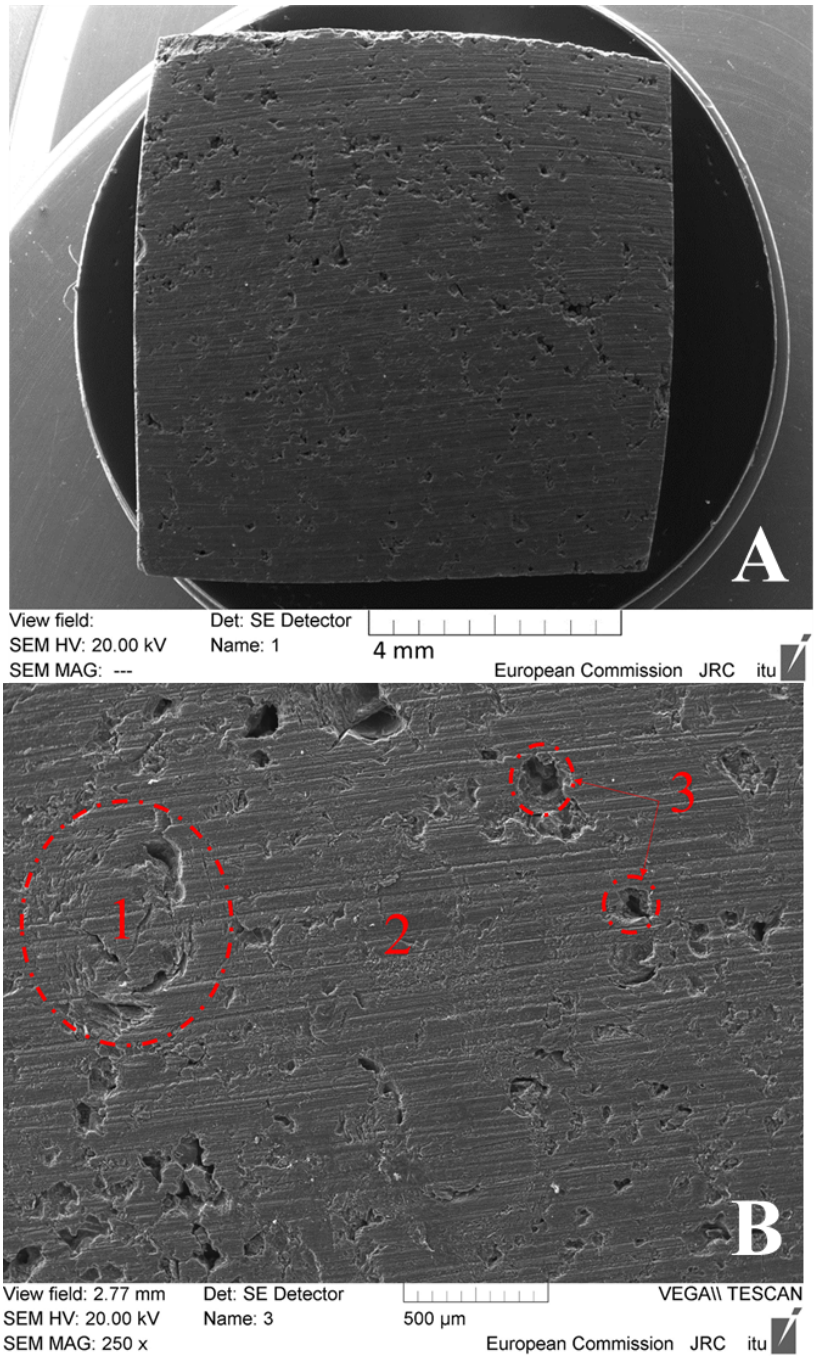

Figure 2- Secondary electron microscopy (SEM) images of the vertical cross-section of an IM1-24 graphite pellet. (A) Image shows the entire sample. (B) Image represents a zoom-in at a random location taken from the upper image. 1 - Gilsocarbon filler particle; 2 - Matrix composed of graphitised binder material; 3 - Pores of varying size and shape.

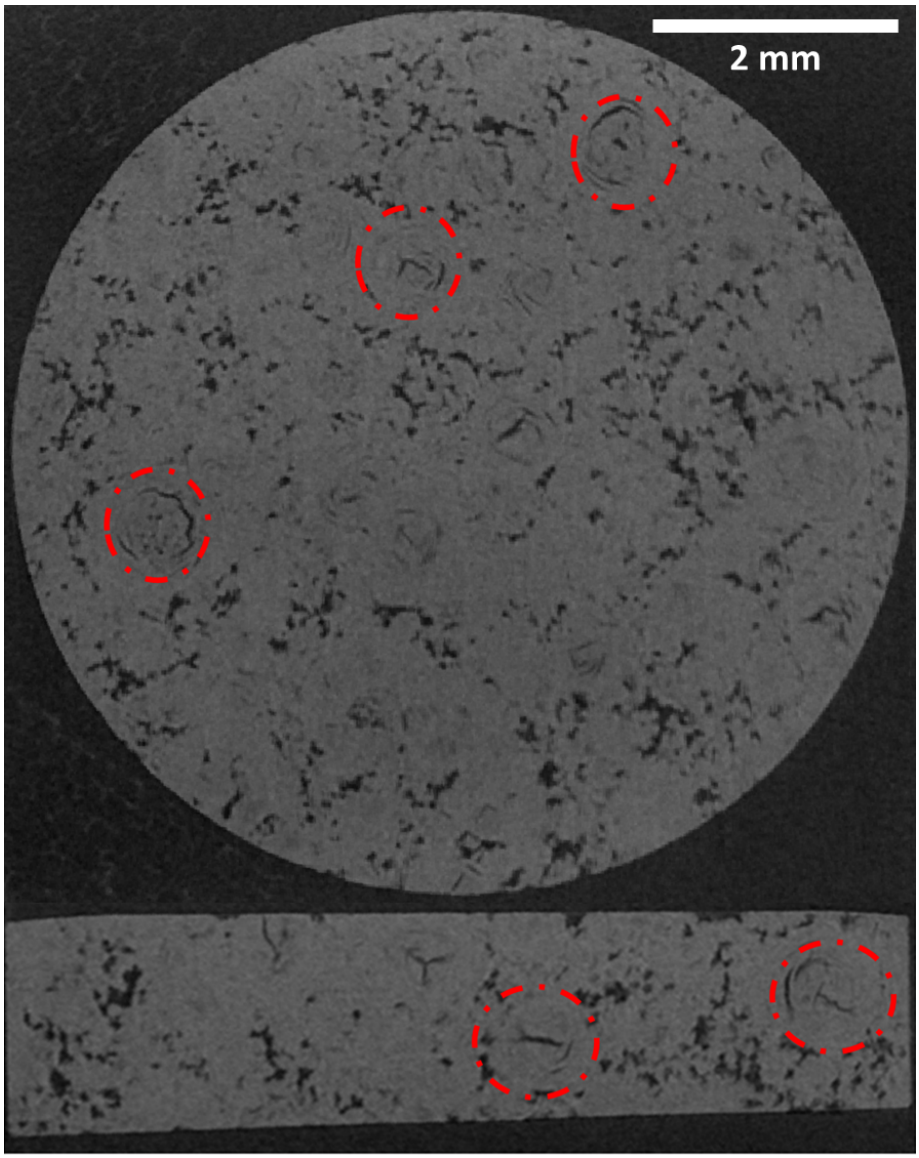

Figure 3 - X-Ray computed tomography images of an IM1-24 graphite pellet. The upper image represents the horizontal cross-section of the pellet while the lower image shows the vertical cross-section. The red dotted lines represent a few of the Gilsocarbon filler particles.

3.2. Thermal property measurements

In this section high-temperature measurements are presented for the following properties - spectral emissivity, thermal conductivity, specific heat and thermal diffusivity. The latter three properties have been plotted for two orthogonal directions. (Please refer to Tables A1 to A5 in the Appendix for the numerical values of the measurements.)

In Figure 4 spectral emissivity measurements are presented in the temperature range 1900 K and 2600 K. The linear fit of the data shows a marginal increase in emissivity from 0.92 at 1800 K to 0.96 at 2600 K. These results were used for the conversion of radiance temperature to black body temperature.

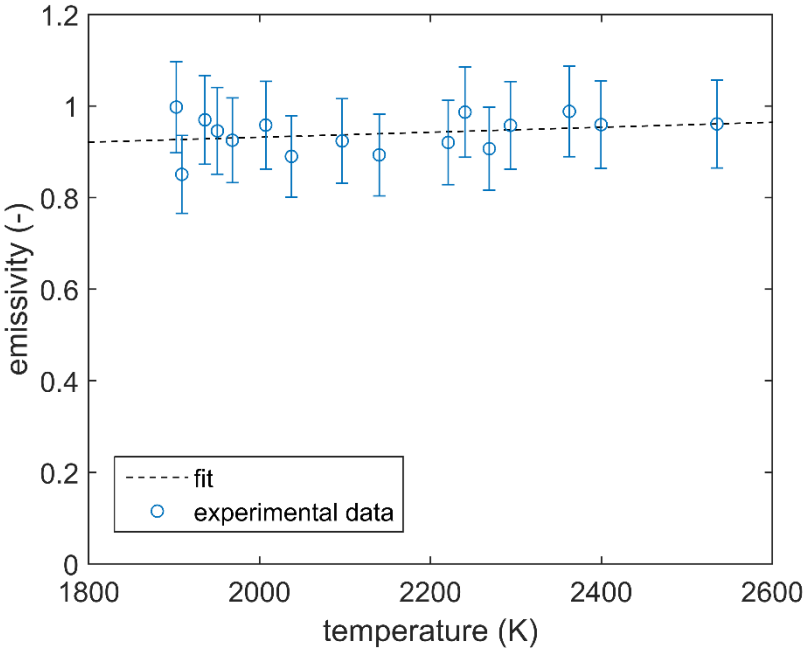

Figure 4 – Spectral emissivity at a laser wavelength of 645 nm as a function of temperature. The dotted line represents a linear fit, its coefficients are reported in Table 2.

Prior to examining the new experimental results of thermal conductivity, a function is proposed for the variation of thermal conductivity with temperature. Even though approximate, this model is based on the physical mechanisms responsible for the thermal transport in the material.

Graphite is a semi-metal, which means its Fermi level lies just above the conduction band. As a result, a minor portion of the electrons in the material are delocalised. These free charge carriers can contribute to properties such as electrical conductivity and thermal conductivity. Additionally, crystal vibrations also play a significant role in the evolution of thermal conductivity with temperature. Throughout this study, these two contributions are addressed as the electronic and lattice terms, respectively. Based on these mechanisms the following expression is used:

$$k_{tot} = k_l + k_{el} \quad (1)$$

where k_l is the lattice contribution and k_{el} is the electronic contribution. According to the Wiedmann-Franz law the electronic term can be expanded as follows:

$$k_{el}(T) = \sigma(T) L T \quad (2)$$

where σ is the electrical conductivity (S m^{-1}), L is the Lorentz number ($W\,\Omega\,K^{-2}$) and T is temperature (K). The Lorentz number recommended by Pavlov et al.[14] has been used ($L = 2.00 \times 10^{-8}\,W\,\Omega\,K^{-2}$). The electrical conductivity is approximated via an empirical function (see equation (3)). This function was deduced in a previous study[14] from the electrical resistivity data of Taylor and Groot[18]. It is important to note that this function is valid for temperatures above 1700 K[14]. This

simplification can be considered acceptable, since the electronic term is relatively small at lower temperatures.

$$\sigma(T) = \left(\frac{1}{2.15 \times 10^{-1} T + 5.56 \times 10^{2}}\right) \times 10^{8} \quad (3)$$

where the factor 10^8 is a unit conversion factor from $\mu\Omega^{-1}$ cm^{-1} to Ω^{-1} m^{-1}. (note: This factor was erroneously omitted in the study of Pavlov et al.[14], however it can be retrieved from the data presented by Taylor and Groot[18]). The lattice term is approximated via the following relationship:

$$k_l = \frac{1}{A + BT} \quad (4)$$

where A (W^{-1} m K) and B (W^{-1} m) are fitting constants, which have been obtained from the new experimental results (A = 5.08119×10^{-4} and B = 1.32025 ×10^{-5}). The overall fit is shown in Figure 5 and given by equation (5).

$$k_{tot} = \frac{2T}{2.15 \times 10^{-1} T + 5.56 \times 10^{2}} + \frac{1}{5.08119 \times 10^{-4} + 1.32025 \times 10^{-5} T} \quad (5)$$

From Figure 5, it is evident that thermal conductivity decreases in the temperature range 500 K to 2500 K. Furthermore, Figure 5A shows that no significant differences were observed between the two orthogonal measurement directions. Figure 5B shows that the electronic contribution only becomes significant at higher temperatures (from ≈ 3% of k_{tot} at 1000 K to ≈ 14 % at 2500 K). Additionally, no variations in the properties were observed as a result of thermal cycling, although the laser flash measurements are relatively quick (of the order of seconds or minutes at most). Longer heating durations would be needed to be able to reach firm conclusions regarding thermal cycling.

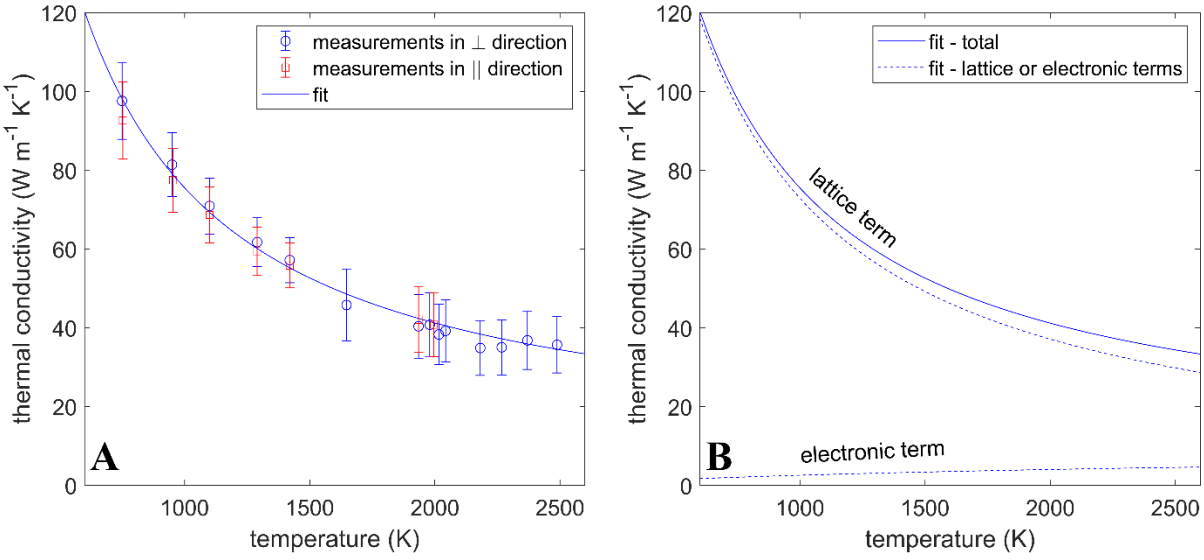

Figure 5 – Thermal conductivity of IM1-24 graphite as a function of temperature: (A) thermal conductivity measurements in two perpendicular directions alongside a fit to the data; (B) comparison of the fitted function and its constituent terms – electronic and lattice.

The measured specific heat values are shown in Figure 6. Within experimental error no differences are observed between the two measurement directions. While it is possible that specific heat may increase slightly in the temperature range 1600 K to 2500 K, within measurement uncertainty, this property can be considered invariant across this temperature range.

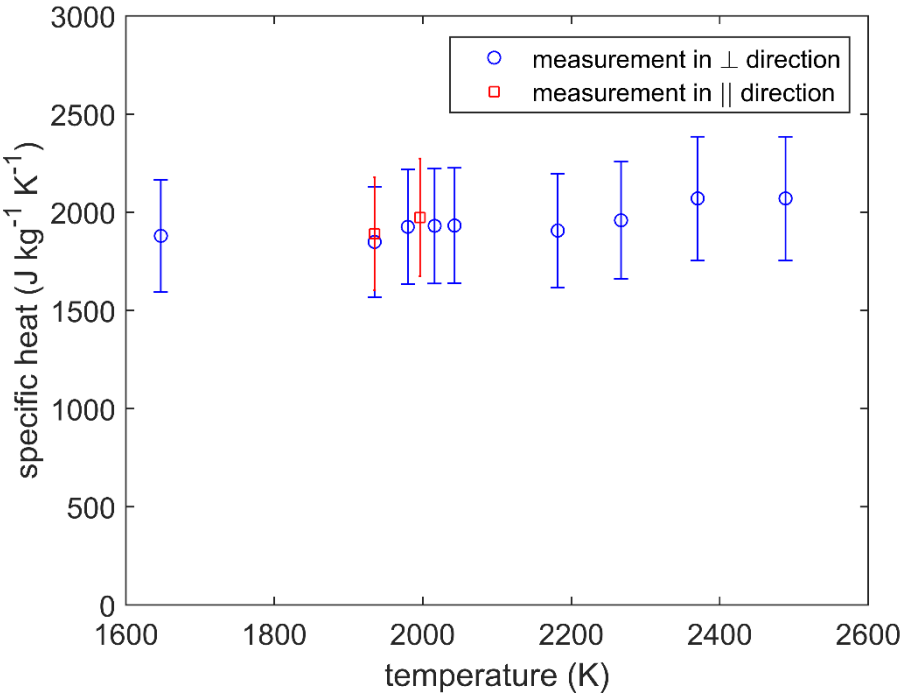

Figure 6 – Specific heat capacity as a function of temperature for two orthogonal directions.

Figure 7 shows the derived thermal diffusivity values as a function of temperature in the two different measurement directions. As for thermal conductivity, no directional dependence of the property was observed. The property decreases with respect to temperature from approximately 3.2 × 10^{-5} m^2 s^{-1} at 1000 K to 0.9 × 10^{-5} m^2 s^{-1} at 2500 K.

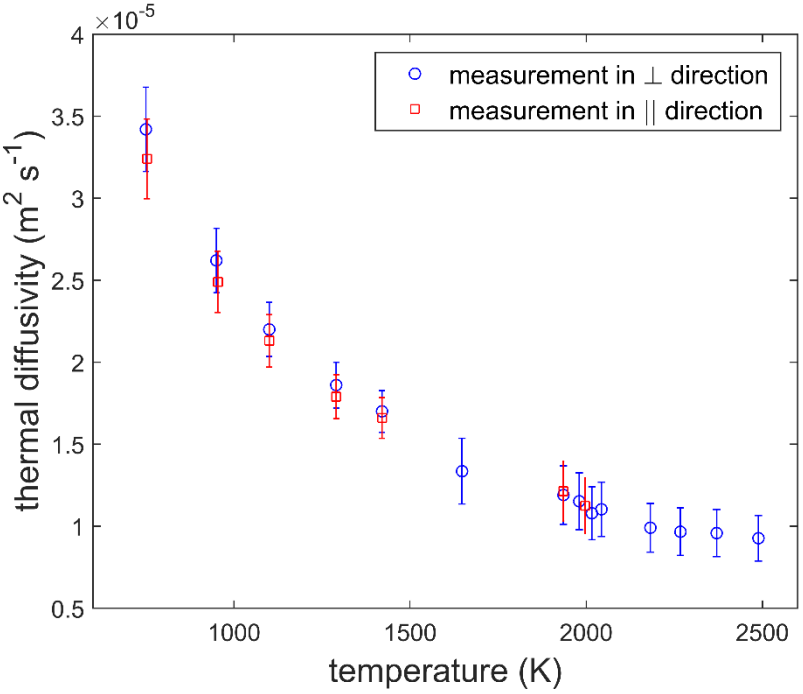

Figure 7 – Thermal diffusivity of IM1-24 graphite in two orthogonal directions.

3.3. Comparison of new results to available literature

In this section some of the newly measured results for nuclear graphite of type IM1-24 are compared to other grades of isotropic graphite – isostatically pressed and POCO AXM-5Q. Additionally, a solid state physics model is applied for comparison and to gain insight into the underlying physical processes.

Figure 8 demonstrates good agreement between the new results and the literature data on isostatically pressed graphite. The measurements performed on POCO graphite exhibit higher values, though still within the measurement uncertainty of the current results. The model proposed by Pavlov et al.[14] is in good agreement with all experimental data. It shows specific heat increases as a function of temperature up to 1000 K, from 0 J kg^{-1} K^{-1} at 0 K, to 1800 J kg^{-1} K^{-1} at 1000 K. At higher temperatures, the increase in specific heat with respect to temperature reduces and the curve flattens with only a relatively small increase observed between 2000 K and 2800 K.

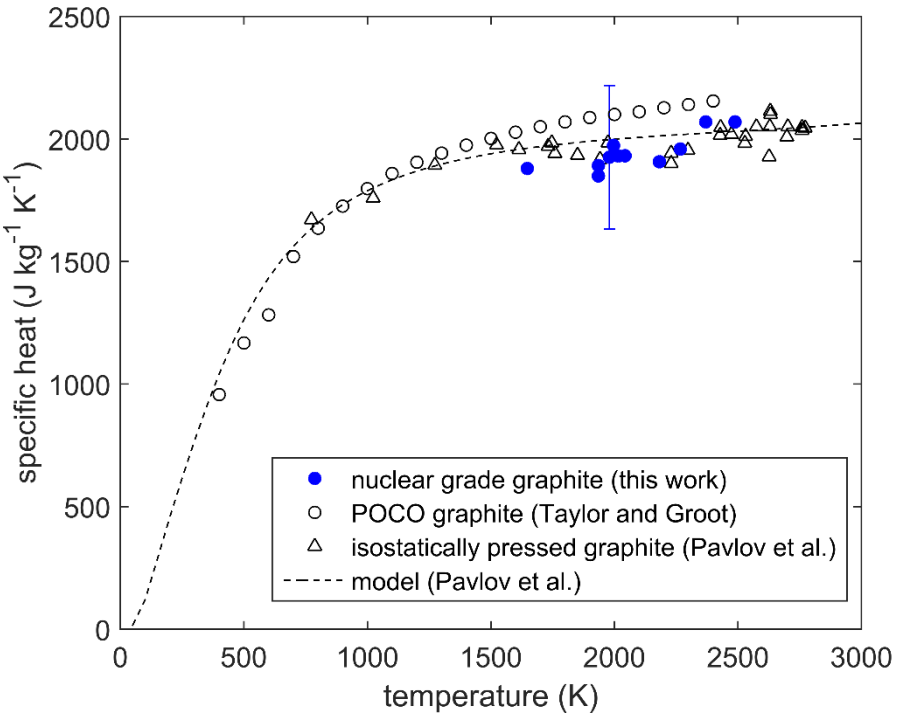

Figure 8 – Specific heat capacity as a function of temperature. The measurements performed in this work are compared to the experimental results of Taylor and Groot[18]*, Pavlov et al.*[14] *and assessed against the model proposed by Pavlov et al.* [14] *The blue error bar is indicative of a relative error of 20% on the current work's results (equivalent to two standard deviations).*

In Figure 9, the new measurements of thermal conductivity are compared to a nearly identical type of isotropic graphite measured by Taylor et al.[19] (Gilsocarbon A), as well as existing data sets on POCO graphite and isostatically pressed graphite. The lower temperature measurements in this study are in good agreement with the higher temperature measurements reported by Taylor et al.[19] The new results tend to be systematically higher compared to the POCO and isostatically pressed graphite albeit within the error bar at higher temperatures though not at lower temperatures. Isostatically pressed graphite exhibits the lowest values amongst the three material types. Furthermore, with increasing temperature the thermal conductivity differences between the graphite grades appear to decrease. All thermal conductivity values provide evidence for a systematic decrease in the value of the property in the examined temperature range (500 K to 2800 K). Furthermore, the model of Pavlov et al.[14] has been applied, in order to compare it to the new set of measurements. The model tends to capture correctly the decreasing trend of thermal conductivity. As previously shown by Pavlov et al.[14], the theoretical results agree with the experiments performed on isostatically pressed graphite.

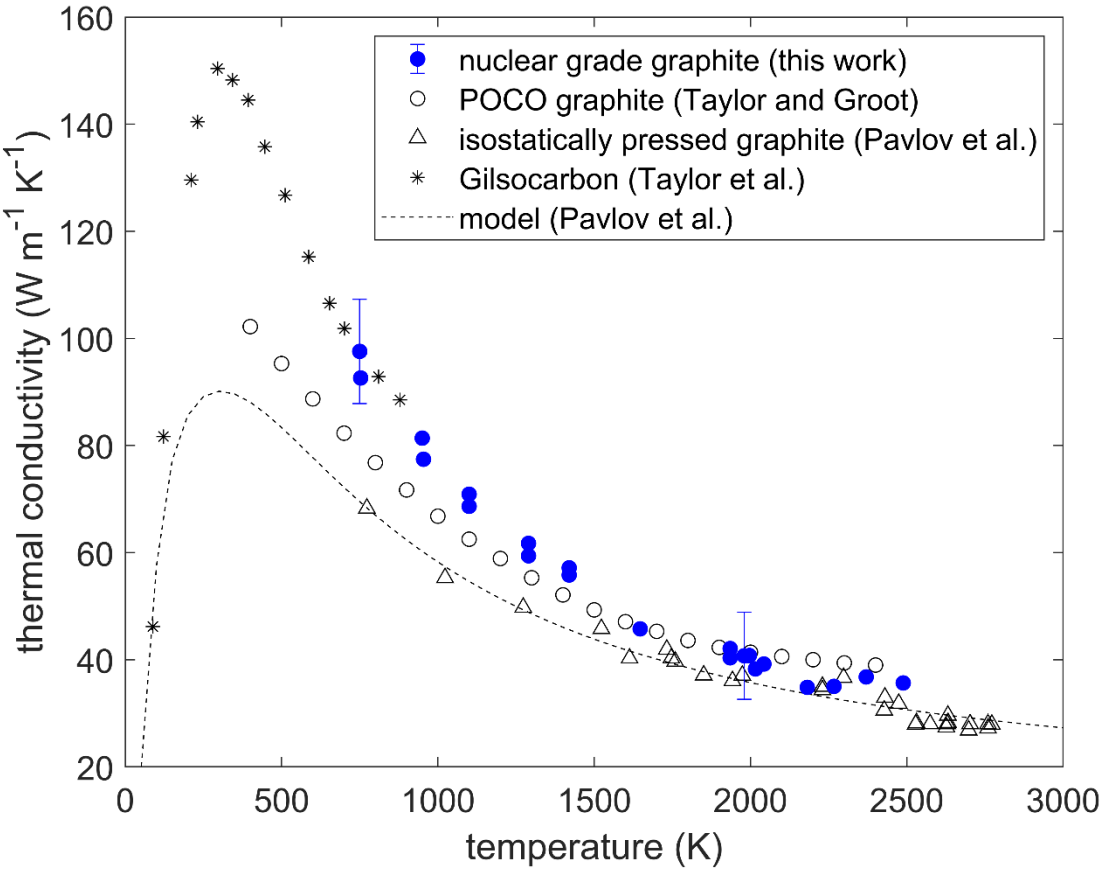

Figure 9 – Thermal conductivity as a function of temperature. The experimental data presented in this work is compared to the measurements of Taylor et al.[19], Taylor and Groot[18], Pavlov et al.[14] and the model proposed by Pavlov et al. [14]. The blue error bar is indicative of a relative error of 20% on the current work's results (equivalent to two standard deviations).

4. Discussion

4.1. Directional dependence of the thermal properties for IM1-24 type graphite

From the data presented in Figure 5 to Figure 7, it is clear that the properties of the AGR graphite are, to within experimental error, identical in two orthogonal directions over the studied temperature range. This is consistent with the reported isotropy in previous studies at lower temperatures[20]. The directional independence of thermal conductivity can be linked to the graphitic microstructure. In Figure 2 and Figure 3 the filler particles and graphitised binder matrix can be observed. The filler particles are characterised by lenticular pores and cracks along the particle circumference. These cracks have been characterised by Mrozowski[21–23]. They are parallel to the basal plane of the hexagonal crystal structure of graphite. These cracks derive from the difference in thermal expansion coefficients in the 'a' and 'c' directions of the hexagonal unit cell. The graphitic planes extending around the circumference of the filler spheres (along the Mrozowski cracks) impact the thermal conductivity tensor of these particles. The principal components of this tensor would be different in the radial and hoop directions, respectively. However, the existence of spherical symmetry means the particles do not exhibit a preferential orientation with respect to the direction of the heat flow. This is confirmed by the independence of thermal conductivity with respect to the direction of measurement. Furthermore, specific heat exhibits no directional dependence as it is a bulk (volumetric) property and is, therefore, scalar.

4.2. Comparing the new measurements to the open literature and condensed matter theory

Figure 8 shows the good agreement between the new measurements of specific heat capacity, previous work and the model. Specific heat increases up to 1000 K and then begins to saturate due to the absence of higher frequency phonon states. The relatively small linear ascent at temperatures above 2000 K is due to electronic contributions. A defect contribution would not be expected at temperatures below 3000 K as the formation energies of Frenkel pairs in graphite are very high (10.2 eV)[24].

Figure 9 compares the new measurements of the thermal conductivity of IM1-24 type graphite to other isotropic types of graphite. The Gilsocarbon measurements reported by Taylor et al. at around 750 K agree very well with the measurements performed on the Gilsocarbon graphite in this work. However, it is clear that significant differences exist between the three types of isotropic grades of graphite. Isostatically pressed graphite exhibits the lowest values of thermal conductivity at temperatures between approximately 750 K and 1500 K, followed by POCO AXM-5Q, with the new results on the

IM1-24 samples being the highest. At temperatures above 2000 K these differences appear to be smaller in magnitude. Possible reasons could include different impurity content, a possible degree of anisotropy in POCO graphite and isostatically pressed graphite or a different microstructure (e.g. different grain size distribution, porosity size and shape). It must be noted that a high purity content has been quoted for all these different materials[14,20,25] and hence it is unlikely for impurities to be the source of the observed differences. The thermal conductivities of POCO AXM-5Q and isostatically pressed graphite have been examined in different directions over a limited temperature range[25,26]. The reported results in these studies show isotropic behaviour of thermal conductivity[25,26]. Hence, anisotropy is probably not the reason for the observed discrepancies. This leads us to consider if it is the microstructure of these different materials that is leading to the thermal transport differences. In particular, that pore shape and size are having the most significant effect on the thermo-physical properties[27,28].

The nature of the filler material and fabrication process may have a significant impact on the material properties. During the fabrication of IM1-24 type graphite spherical Gilsocarbon particles are added as the filler material, while for POCO AXM-5Q graphite petroleum coke is used[29], and for isostatic graphite a combination of coke and graphite[30]. In the case of the IM1-24 type material, the presence of large filler particles with circumferentially wound graphitic platelets[31] may assist phonons to propagate along the basal plane of these sheets. Since the in-plane thermal transport is orders of magnitude higher, such a mechanism may provide an efficient path for thermal transport. In comparison, cold isostatically pressed samples do not consist of large filler particles, which is evident from the X-ray tomography results presented in Figure 10A and Figure 10B. This material exhibits crystallites in random orientations (see Figure 10E). Such an initial configuration could constrain the degree of graphitization[32–34] and inhibit the ability of heat to be transported via the strongly conductive basal planes. This could explain the superior thermal conductivity of IM1-24 compared to cold isostatically pressed graphite grades. POCO-AXM graphite contains 5 μm sized filler particles[35] in comparison to the 500 μm Gilsocarbon particles of the IM1-24 type material. A smaller particle size indicates a lower mean free path for phonons traveling along the particle's constituent graphene planes. Hence, it is understandable that POCO AXM specimen would exhibit a lower thermal conductivity compared to the IM1-24 samples.

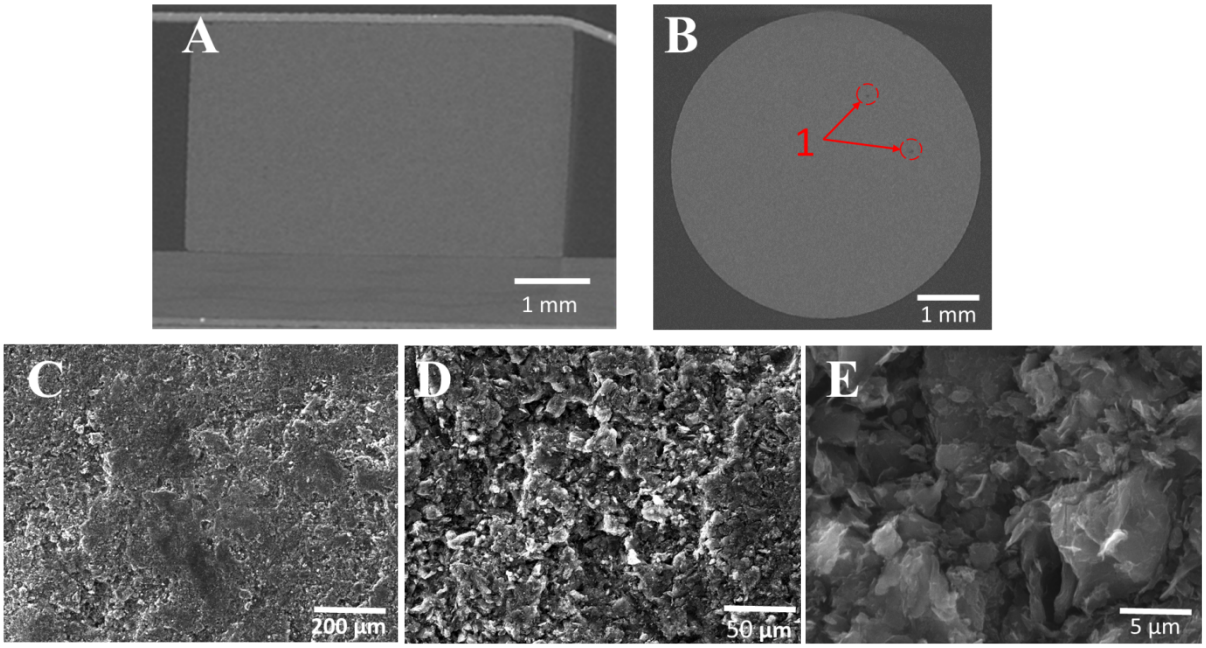

Figure 10 – Microstructural characterisation of isostatically pressed graphite pellets performed in this work the thermal conductivity of these specimen was examined in previous studies[14,15,17] (diameter: 5 mm / thickness: 3 mm / density: 1.81 g/cm^3). A) Vertical cross section of the sample measured via XRT; B) Horizontal cross section of the sample measured via XRT. The red circles associated with feature "1" mark microscopic pores with size comparable to the resolution limit of the device; C) SEM image of the sample showing surface porosity and a fine grain structure; D) SEM image (magnification of C) showing some partial grain structure; E) SEM image (magnification of D) showing randomly oriented lamellae.

In Figure 8 the prediction made using the solid state physics model of Pavlov et al.[14] is compared to the various experimental data sets from the different grades of isotropic graphite. The model assumes a homogeneous quasi-isotropic structure, which is not the case for IM1-24. However, randomly oriented lamellae are observed in fine grained isostatically pressed graphite (see Figure 10E), in accordance with the model assumption. Even though limited, the model does offer insight into certain physical mechanisms and their importance. The decrease in thermal conductivity as a function of temperature can be attributed predominantly to inelastic phonon-phonon interactions. Grain boundaries reduce the phonon mean free path only slightly and this reduction becomes less influential at higher temperatures. The interaction of phonons with electrons, as well as C^{13} impurities also leads to a minor reduction in thermal conductivity, which is most pronounced at near-ambient temperatures. Finally, it is clear that a multi-scale model would be needed to investigate all mechanisms for thermal transport at the different length scales.

5. Conclusions

- For the first time high temperature measurements (between 750 K and 2500 K) were performed to determine the thermal conductivity, thermal diffusivity, specific heat and spectral emissivity of unirradiated AGR graphite samples (type IM1-24) from Hartlepool and Dungeness power stations.

- All thermal properties were investigated in two orthogonal directions. The results showed the effective macroscopic thermal conductivity to be isotropic. This is consistent with the structure of the filler particles, which consist of concentrically aligned graphitic platelets.

- The solid state physics model for thermal conductivity is consistent with inelastic phonon scattering (lattice vibrations) dominating the high temperature behavior of graphite (above approximately 1000 K) followed by contributions from thermally mobilized electrons. However, the model does not capture the multi-scale nature of thermal transport in IM1-24 graphite.

Disclosure statement

Acknowledgements

The European Commission is acknowledged for the funding and experimental facilities provided to support the current work.

Appendix

Figure A1 compares the measured values of thermal conductivity obtained from specimen machined from the Dungeness and Hartlepool billets.

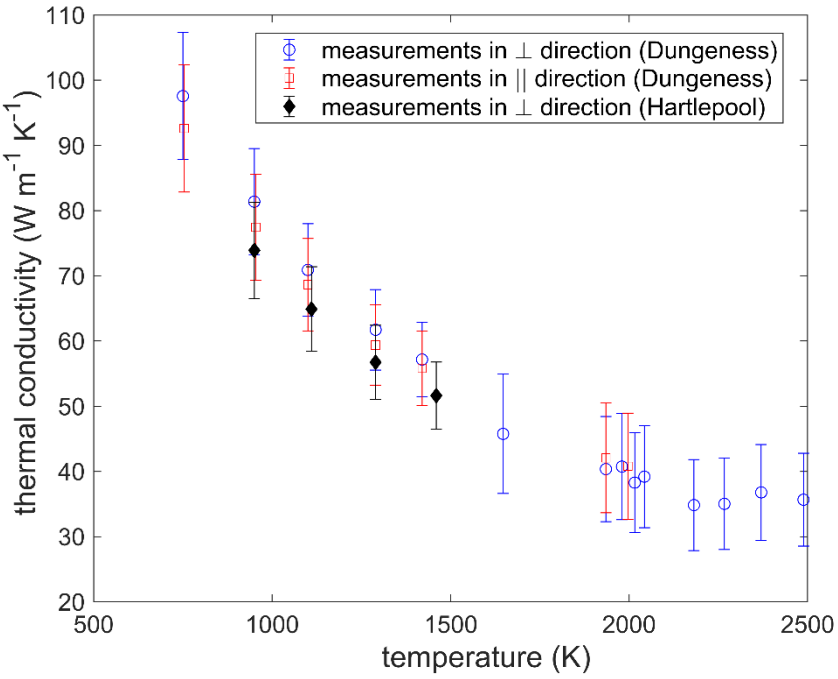

Figure A1 – Comparison between the thermal conductivity measurements obtained from the Dungeness and Hartlepool specimen as afunction of temperature

Tables A1 to A4 contain all measured values of thermal diffusivity, specific heat, thermal conductivity and spectral emissivity at 645 nm.

Table A1 – Measuremetns obtained in the perpendicular (⊥) direction via the Continuous wave Laser Surface Heating (CLASH) apparatus.

Temperature (K)	Thermal conductivity (W m^{-1} K^{-1})	Specific heat (J kg^{-1} K^{-1})	Thermal diffusivity (mm^2 s^{-1})
1980	40.7	1925.6	12.3
2370	36.8	2069.6	10.4
2488	35.7	2069.6	10.1
2016	38.3	1930.3	11.5
2267	35.0	1959.5	10.4
1647	45.8	1880.0	14.0
1935	40.36	1849.2	12.6
2043	39.19	1932.0	11.8
2182	34.84	1906.7	10.6

* thermal diffusivity is calculated via the equation $\alpha = \frac{k}{\rho \times c_P}$ (the correlations in Table 2 were used for the temperature dependent density)

Table A 2 Measuremetns obtained in the parallel (∥) direction via the Continuous wave Laser Surface Heating (CLASH) apparatus.

Temperature (K)	Thermal conductivity (W m^{-1} K^{-1})	Specific heat (J kg^{-1} K^{-1})	Thermal diffusivity * (mm^2 s^{-1})
1935	42.09	1891.4	12.9
1996	40.78	1973.3	12.0

* thermal diffusivity is calculated via the equation $\alpha = \frac{k}{\rho \times c_P}$ (the correlations in Table 2 were used for the temperature dependent density)

Table A3 - Measuremetns obtained in the parallel (⊥) direction via the Continuous wave Laser Surface Heating (CLASH) apparatus.

Temperature (K)	Thermal conductivity (W m^{-1} K^{-1})	Specific heat (J kg^{-1} K^{-1})	Thermal diffusivity (mm^2 s^{-1})
750	97.6	1613.5	34.2
950	81.4	1762.3	26.2
1100	70.9	1833.5	22.0
1290	61.7	1894.7	18.6
1420	57.2	1924.7	17.0

* thermal conductivity is calculated via the equation $k = \alpha \times \rho \times c_P$ (the correlations in Table 2 were used for the temperature dependent density)

** specific heat is calculated based on the validated model developed by Pavlov et al.[14]

Table A4 - Measuremetns obtained in the parallel (∥) direction via the Continuous wave Laser Surface Heating (CLASH) apparatus.

Temperature (K)	Thermal conductivity* (W m^{-1} K^{-1})	Specific heat** (J kg^{-1} K^{-1})	Thermal diffusivity (mm^2 s^{-1})
753	92.6	1616.4	32.4

954	77.4	1764.6	24.9
1100	68.6	1833.5	21.3
1290	59.4	1894.7	17.9
1420	55.8	1924.7	16.6

* thermal conductivity is calculated via the equation $k = \alpha \times \rho \times c_P$ (the correlations in Table 2 were used for the temperature dependent density)

** specific heat is calculated based on the validated model developed by Pavlov et al.[14]

Table A5 - Measured emissivity as a function of temperature.

Temperature (K)	Emissivity at 645 nm (-)
2362	0.99
2096	0.92
1936	0.97
1968	0.93
2007	0.96
2240	0.99
1903	1.00
2535	0.96
2400	0.96
1951	0.95
2269	0.91
2293	0.96
2037	0.89
2140	0.89
2221	0.92
1909	0.85

References

1. Marsden, B. J. Nuclear graphite for high temperature reactors. in *Gas turbine power conversion systems for modular HTGRs* 177–192 (2001). doi:10.1016/S1872-5805(17)60116-1

2. Maruyama, T. & Harayama, M. Neutron irradiation effect on the thermal conductivity and dimnesional change of graphite materials. *J. Nucl. Mater.* **195,** 44–50 (1992).

3. Nonbøl, E. *Description of the advanced gas cooled type of reactor (AGR)*. (Riso National Laboratory, NKS/RAK2(96)TR-C2, 1996).

4. Kelly, B. T. *The Physics of Graphite*. (Applied Science: London, 1981).

5. Taylor, R., Gilchrist, K. E. & Poston, L. J. Thermal conductivity of polycristalline graphite. *Carbon (1968)* **6,** 537–544 (1968).

6. Slack, G. A. Anisotropic thermal conductivity of pyrolitic graphite. *Phys. Rev.* **127,** 694–701 (1962).

7. Tsang, D. K. L. & Marsden, B. J. Constitutive material model for the prediction of stresses in irradiated anisotropic graphite components. *J. Nucl. Mater.* **381,** 129–136 (2008).

8. Marlowe, M. O. Elastic properties of three grades of fine grained graphite to 2000 C. 1–30 (1970).

9. Engle, G. B. & Kelly, B. T. Radiation damage of graphite in fission and fusion reactor systems. *J. Nucl. Mater.* **122,** 122–129 (1984).

10. Kelly, B. T. Graphite-the most fascinating nuclear material. *Carbon N. Y.* **20,** 3–11 (1982).

11. Rasor, N. S. & McClelland, J. D. Thermal properties of graphite, molybdenum and tantalum to their destruction temperatures. *J. Phys. Chem. Solids* **15,** 17–26 (1960).

12. Wen, K. Y., Marrow, T. J. & Marsden, B. J. The microstructure of nuclear graphite binders. *Carbon (2008)* **46,** 62–71 (2008).

13. Sheindlin, M., Halton, D., Musella, M. & Ronchi, C. Advances in the use of laser-flash techniques for thermal diffusivity measurement. *Rev. Sci. Instrum.* **69,** 1426–1436 (1998).

14. Pavlov, T., Vlahovic, L., Staicu, D., Konings, R. J. M., Wenman, M. R., Van Uffelen, P. & Grimes, R. W. A new numerical method and modified apparatus for the simultaneous evaluation of thermo-physical properties above 1500 K: A case study on isostatically pressed graphite. *Thermochim. Acta* **652,** (2017).

15. Pavlov, T. R., Staicu, D., Vlahovic, L., Konings, R. J. M., Van Uffelen, P. & Wenman, M. R. A new method for the characterization of temperature dependent thermo-physical properties.

Int. J. Therm. Sci. **124,** (2018).

16. Pavlov, T., Wenman, M. R., Vlahovic, L., Robba, D., Konings, R. J. M., Uffelen, P. Van & Grimes, R. W. Measurement and interpretation of the thermo-physical properties of UO_2 at high temperatures: the viral effect of oxygen defects. *Acta Mater.* **139,** 138–154 (2017).

17. Hay, B., Anhalt, K., Chapman, L., Boboridis, K., Hameury, J., Krenek, S., Vlahovic, L., Fleurence, N. & Beneš, O. Traceability improvement of high temperature thermal property measurements of materials for new fission reactors. *IEEE Trans. Nucl. Sci.* **61,** 2112–2119 (2014).

18. Taylor, R. E. & Groot, H. *Thermophysical Properties of POCO Graphite.* (Properties Research Lab, AFOSR-78-1375, 1978).

19. Taylor, R., Gilchrist, K. E. & Poston, L. J. Thermal conductivity of polycrystalline graphite. *Carbon (1968)* **6,** 537–544 (1968).

20. Middleton, P. M. & Moore, R. W. Role and development of nuclear graphite for gas cooled reactors, with particular reference to the high temperature reactor. in *International Nuclear Industries Fair* 1–15 (Nuclex 72, 1972).

21. Liu, D. & Cherns, D. Nano-cracks in a synthetic graphite composite for nuclear applications. *Philos. Mag.* **98,** 1272–1283 (2018).

22. Mrozowski, S. Mechanical strength, thermal expansion and structure of cokes and carbons. in *1st and 2nd Conferences on Carbon* 31 (1956).

23. Liu, D., Gludovatz, B., Barnard, H. S., Kuball, M. & Ritchie, R. O. Damage tolerance of nuclear graphite at elevated temperatures. *Nat. Commun.* **8,** 1–9 (2017).

24. Li, L., Reich, S. & Robertson, J. Defect energies of graphite: Density-functional calculations. *Phys. Rev. B - Condens. Matter Mater. Phys.* **72,** 1–10 (2005).

25. Sheppard, R. G., Mathes, D. M. & Bray, D. J. *Properties and characteristics of graphite for industrial applications*. (Poco Graphite Inc, 2001).

26. SGL carbon. *Specialty graphites for the photovoltaic industry*. (2015).

27. Ordonez-Miranda, J. & Alvarado-Gil, J. J. Effect of the pore shape on the thermal conductivity of porous media. *J. Mater. Sci.* **47,** 6733–6740 (2012).

28. Li, H., Zeng, Q. & Xu, S. Effect of pore shape on the thermal conductivity of partially saturated cement-based porous composites. *Cem. Concr. Compos.* **81,** 87–96 (2017).

29. Hust, J. G. *A fine-grained, isotropic graphite for use as NBS thermophysical property RM's*

from 5 to 2500 K. (1984). doi:10.15713/ins.mmj.3

30. Shen, K., Huang, Z. H., Hu, K., Shen, W., Yu, S., Yang, J., Yang, G. & Kang, F. Advantages of natural microcrystalline graphite filler over petroleum coke in isotropic graphite preparation. *Carbon N. Y.* **90,** 197–206 (2015).

31. Shen, K., Yu, S. & Kang, F. The microstructure and texture of Gilsocarbon graphite. *Carbon N. Y.* **153,** 428–437 (2019).

32. Oberlin, A. Carbonization and graphitization. *Carbon (1984)* **22,** 521–541 (1984).

33. Harris, P. J. F. Structure of non-graphitising carbons. *Int. Mater. Rev.* **42,** 206–218 (1997).

34. Rannou, I., Bayot, V. & M. Lelaurain. Structural charachterization of graphitization process in pyrocarbons. *Carbon (1994)* **32,** 833–843 (1994).

35. Woodcraft, A. L., Barucci, M., Hastings, P. R., Lolli, L., Martelli, V., Risegari, L. & Ventura, G. Thermal conductivity measurements of pitch-bonded graphites at millikelvin temperatures: Finding a replacement for AGOT graphite. *Cryogenics (Guildf).* **49,** 159–164 (2009).

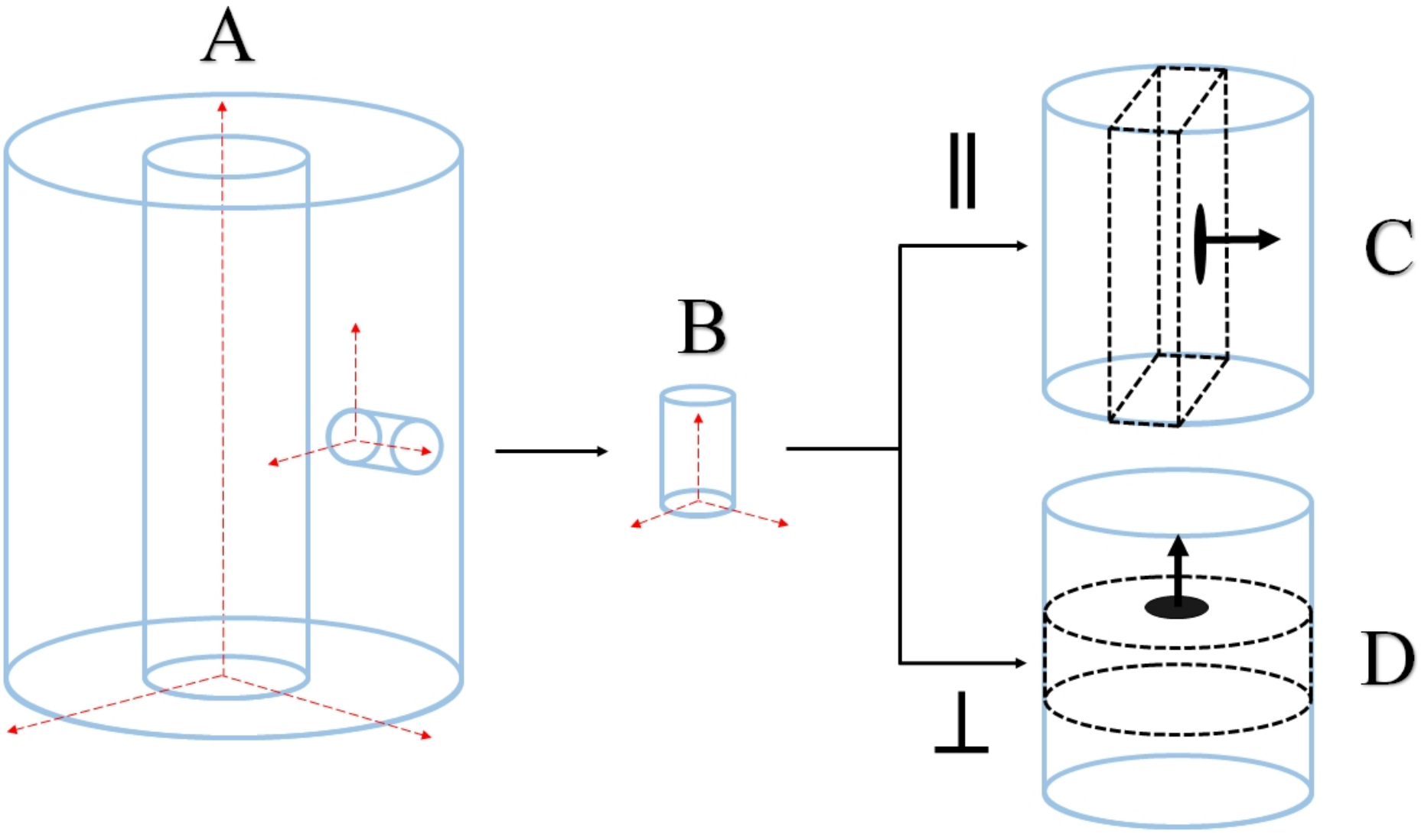
A
B
∥
C
⊥
D

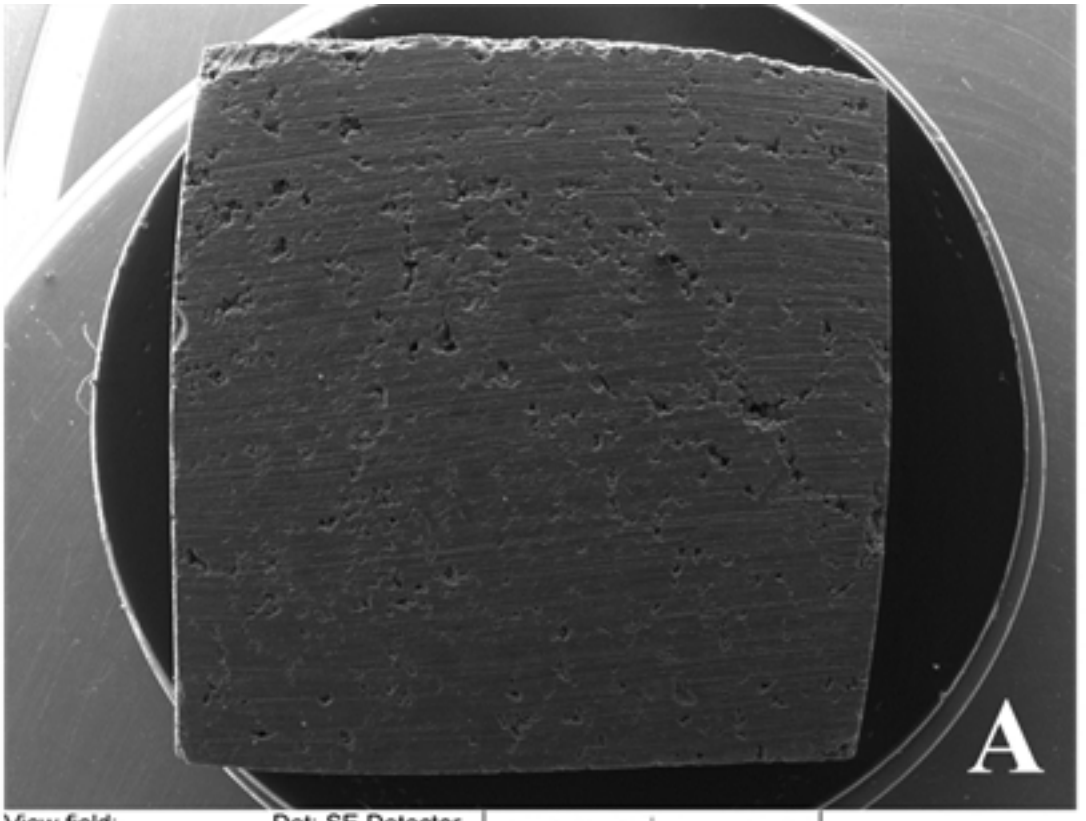
A
View field:
SEM HV: 20.00 kV
SEM MAG: ---
Det: SE Detector
Name: 1
4 mm
European Commission JRC itu

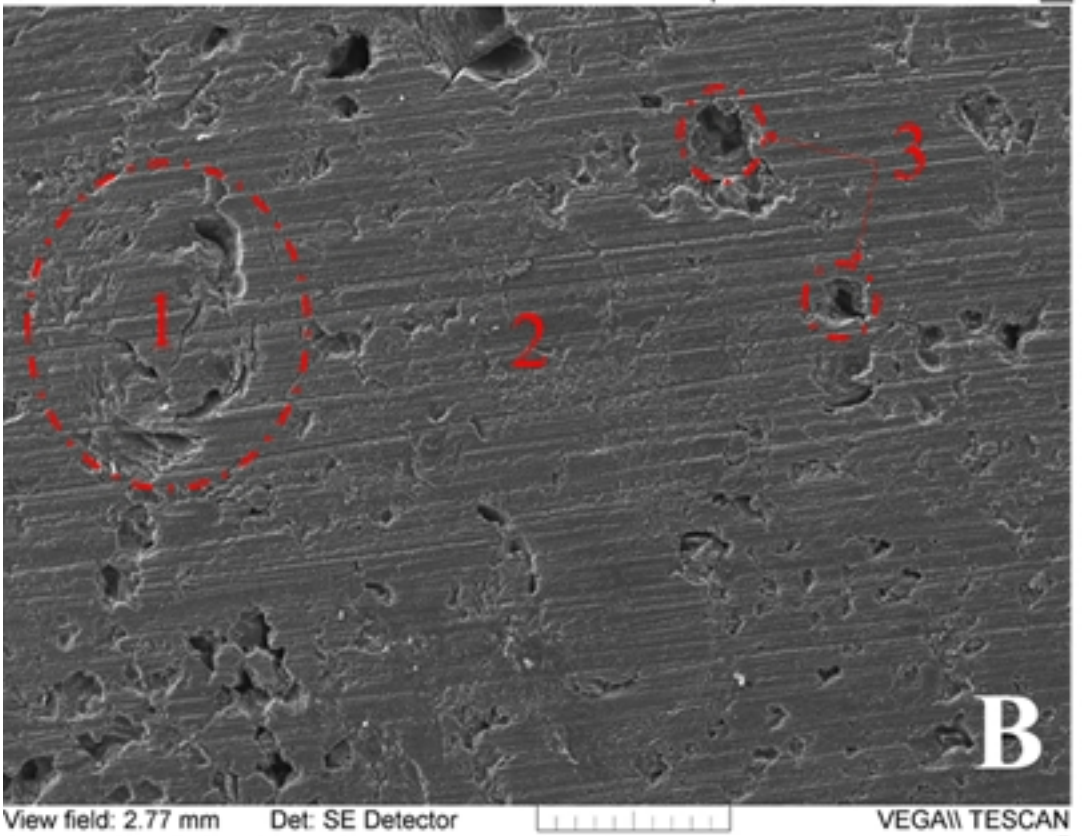
1
2
3
B
View field: 2.77 mm
SEM HV: 20.00 kV
SEM MAG: 250 x
Det: SE Detector
Name: 3
500 µm
VEGA\\ TESCAN
European Commission JRC itu

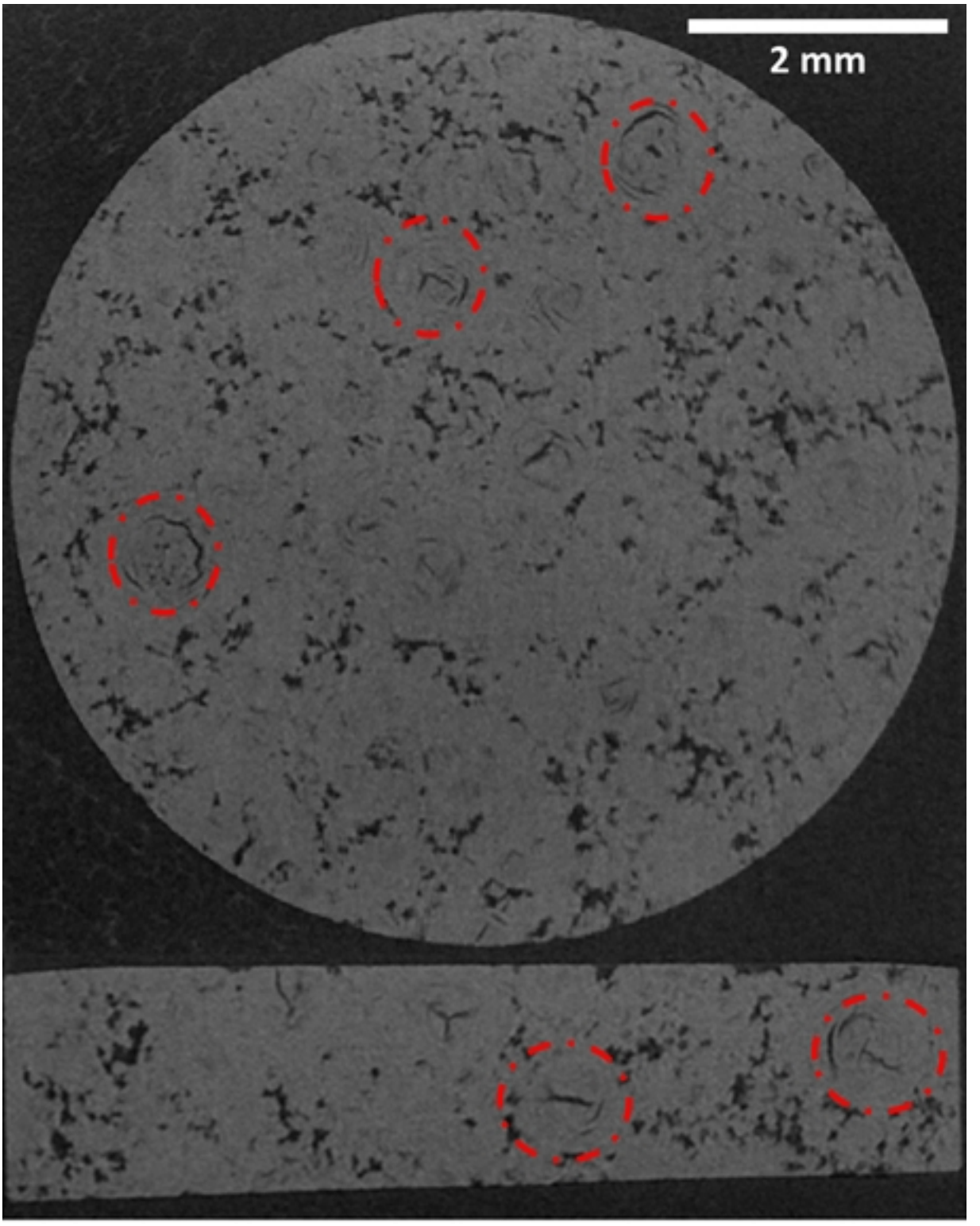
2 mm

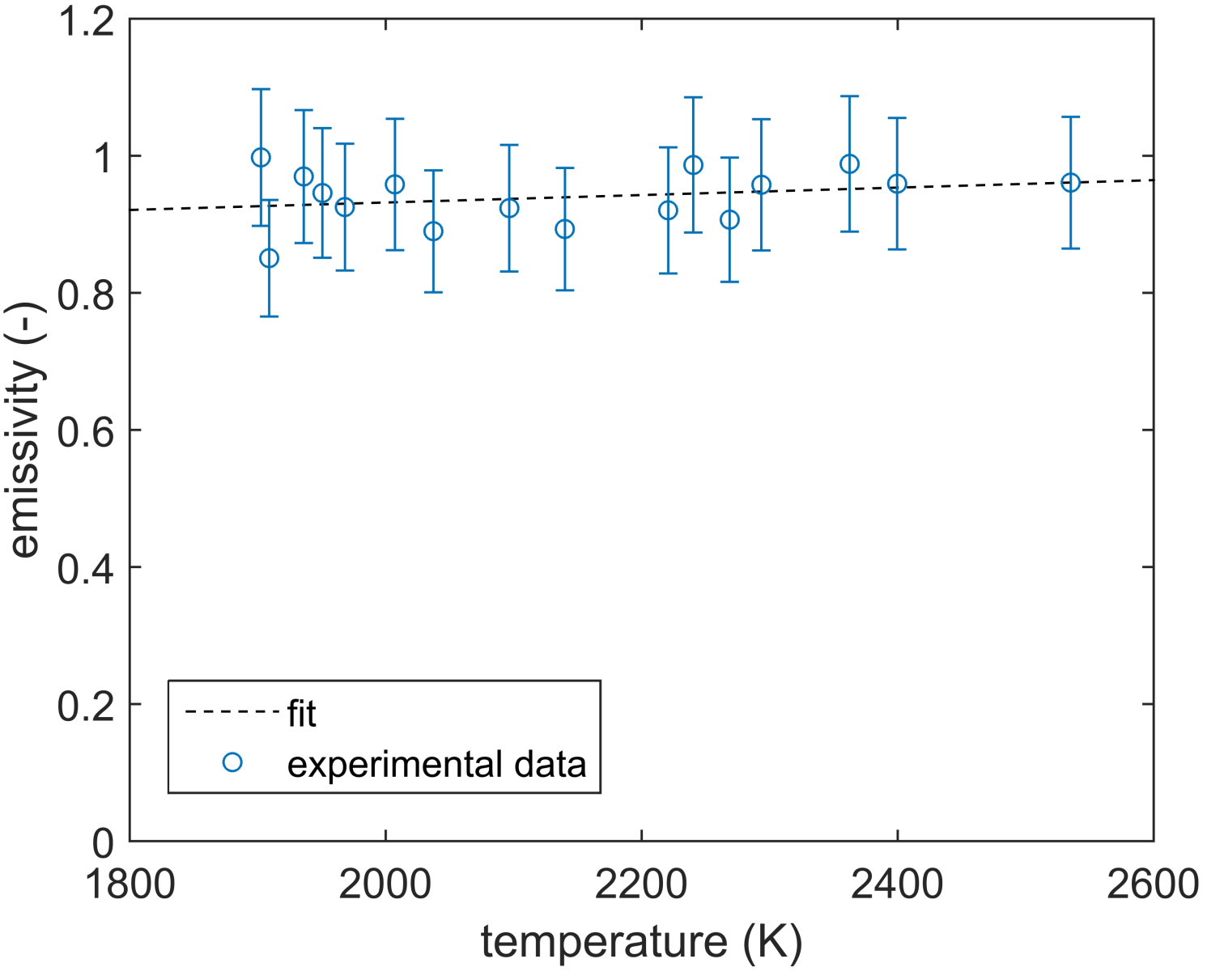
1.2
1
0.8
0.6
0.4
0.2
0
emissivity (-)
1800
2000
2200
2400
2600
temperature (K)
fit
experimental data

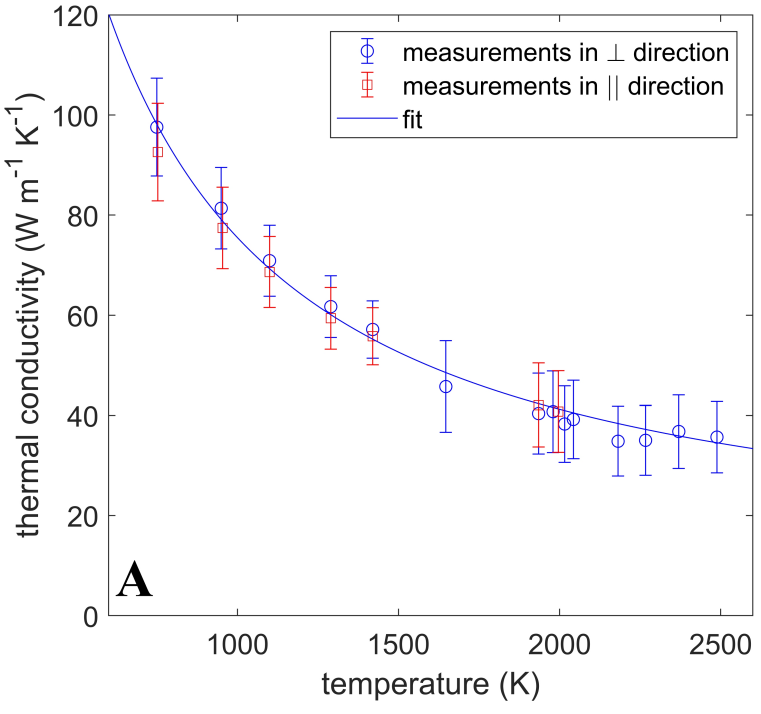
measurements in ⊥ direction
measurements in || direction
fit
thermal conductivity (W m-1 K-1)
temperature (K)
A
0
20
40
60
80
100
120
1000
1500
2000
2500

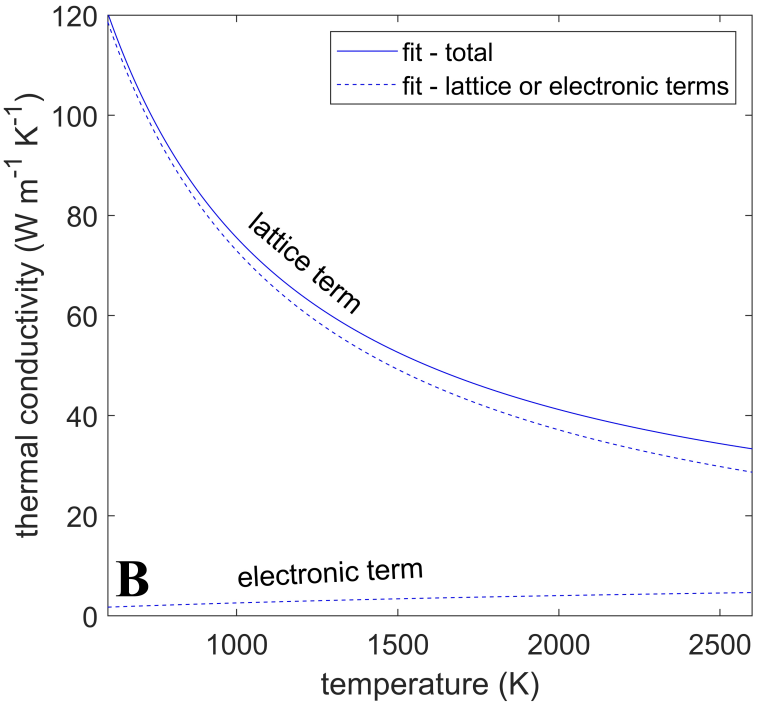
fit - total
fit - lattice or electronic terms
lattice term
electronic term
thermal conductivity (W m-1 K-1)
temperature (K)
B
0
20
40
60
80
100
120
1000
1500
2000
2500

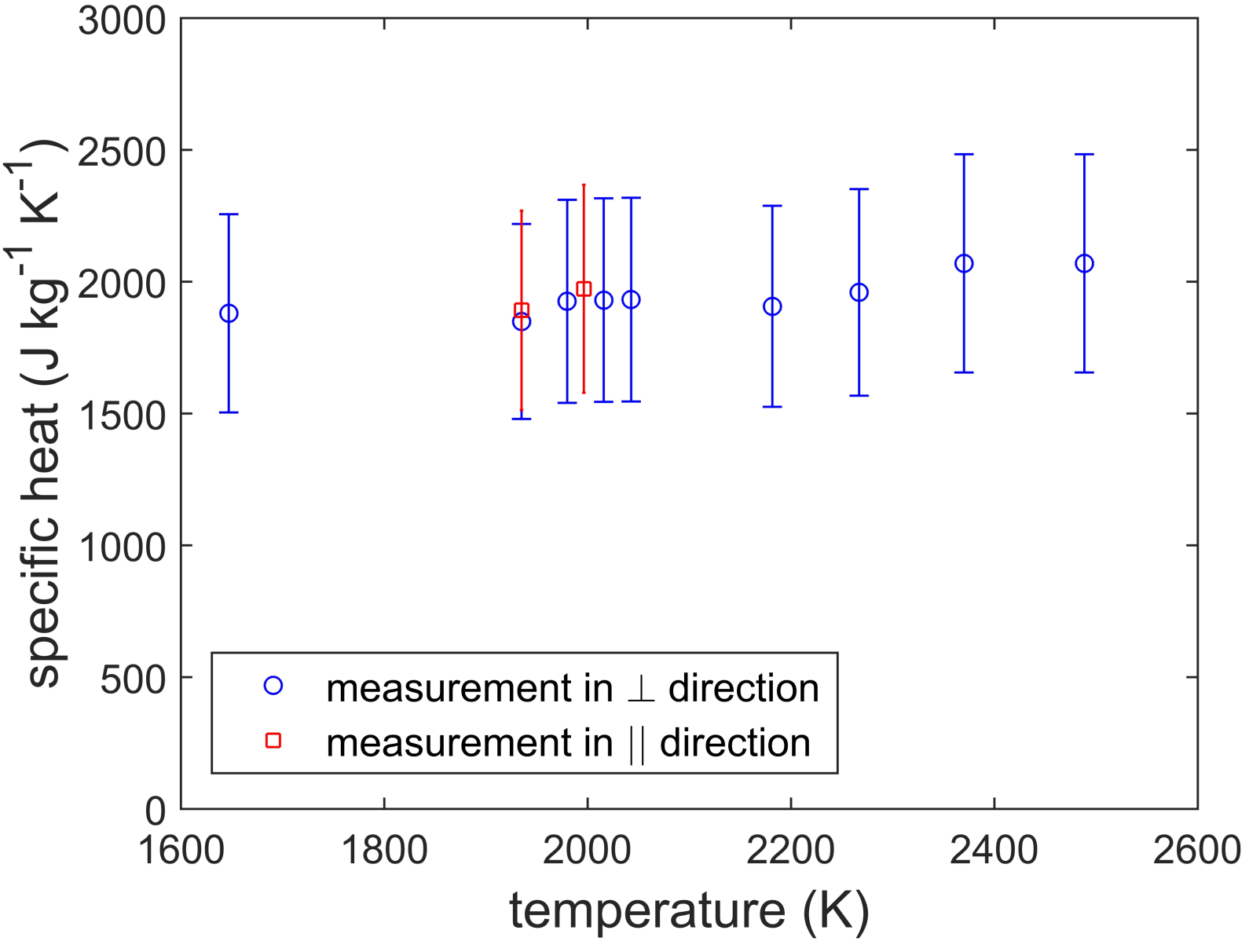
3000
2500
2000
1500
1000
500
0
specific heat (J kg-1 K-1)
1600
1800
2000
2200
2400
2600
temperature (K)
measurement in ⊥ direction
measurement in || direction

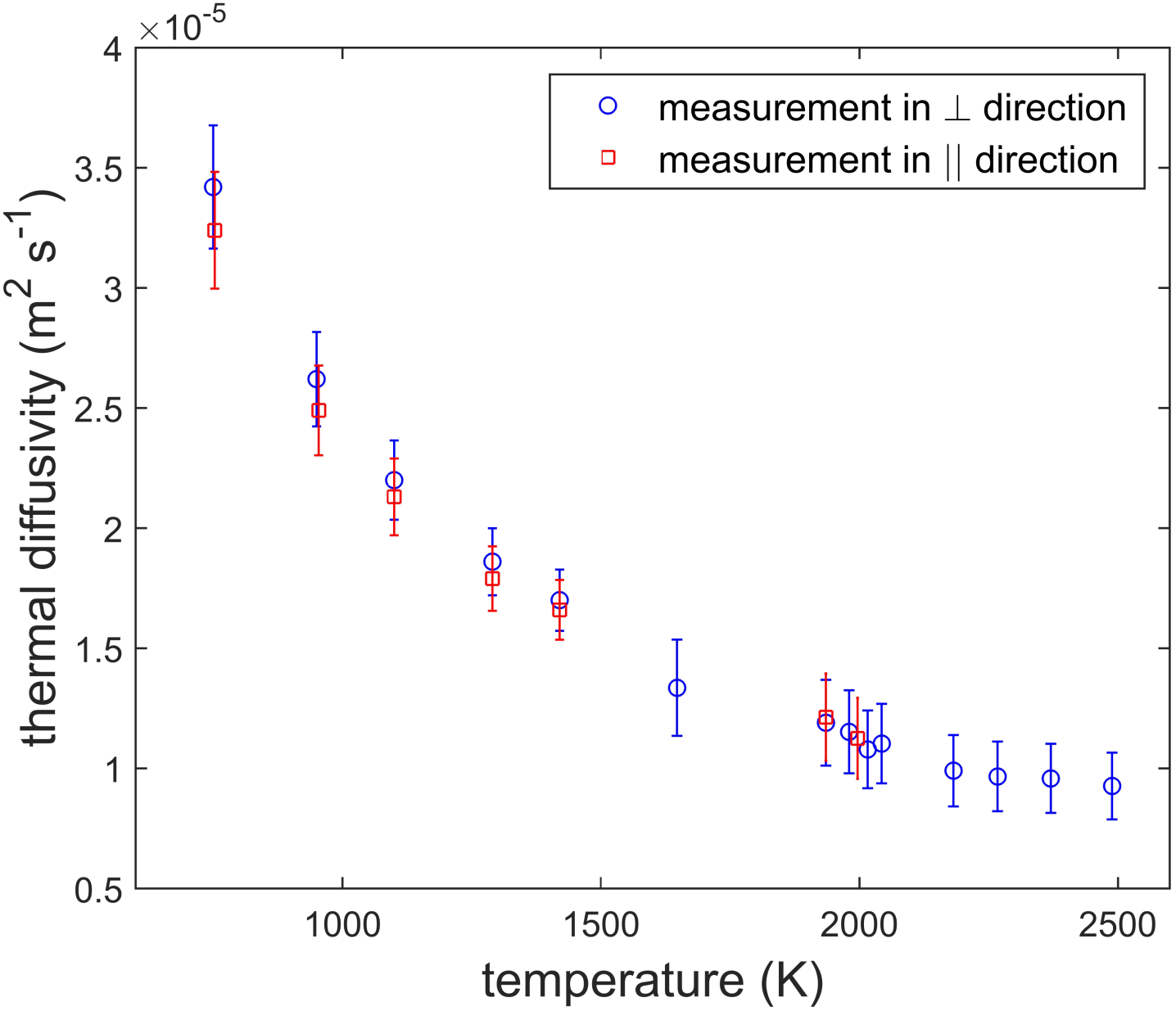
×10^-5
4
3.5
3
2.5
2
1.5
1
0.5
thermal diffusivity (m^2 s^-1)
1000
1500
2000
2500
temperature (K)
measurement in ⊥ direction
measurement in || direction

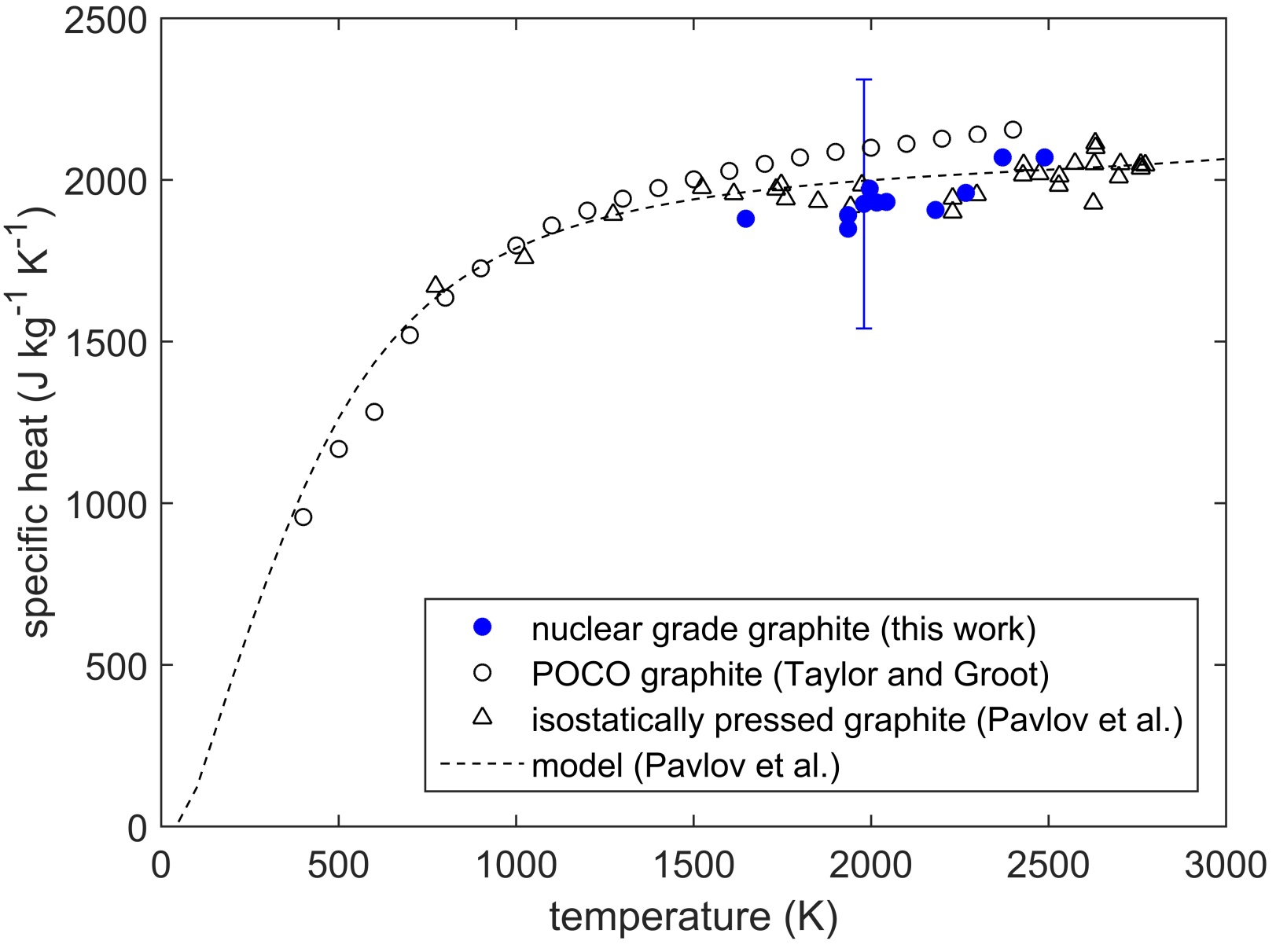
2500
2000
1500
1000
500
0
specific heat (J kg-1 K-1)
0
500
1000
1500
2000
2500
3000
temperature (K)
nuclear grade graphite (this work)
POCO graphite (Taylor and Groot)
isostatically pressed graphite (Pavlov et al.)
model (Pavlov et al.)

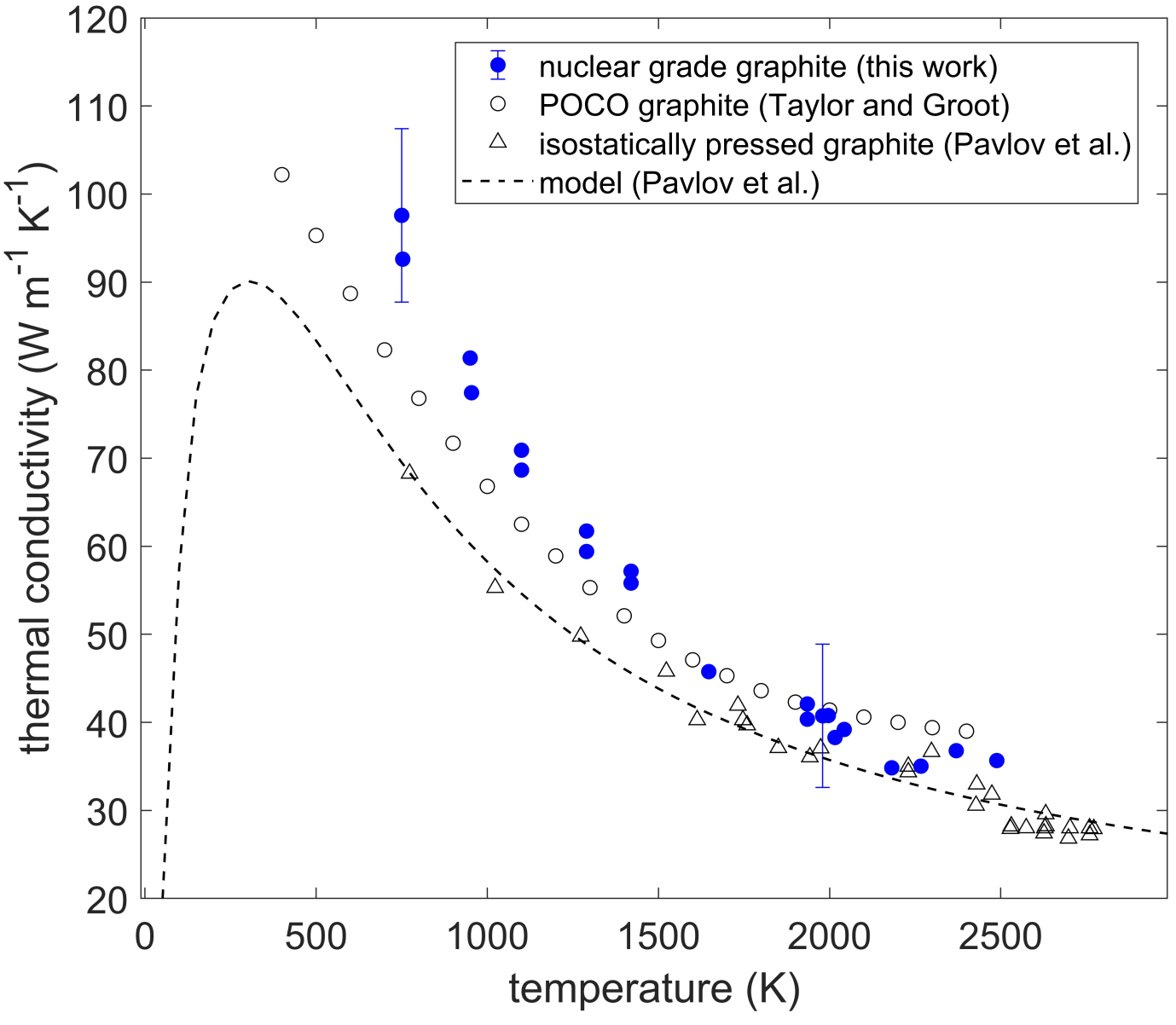
nuclear grade graphite (this work)
POCO graphite (Taylor and Groot)
isostatically pressed graphite (Pavlov et al.)
model (Pavlov et al.)
thermal conductivity (W m-1 K-1)
temperature (K)
120
110
100
90
80
70
60
50
40
30
20
0
500
1000
1500
2000
2500

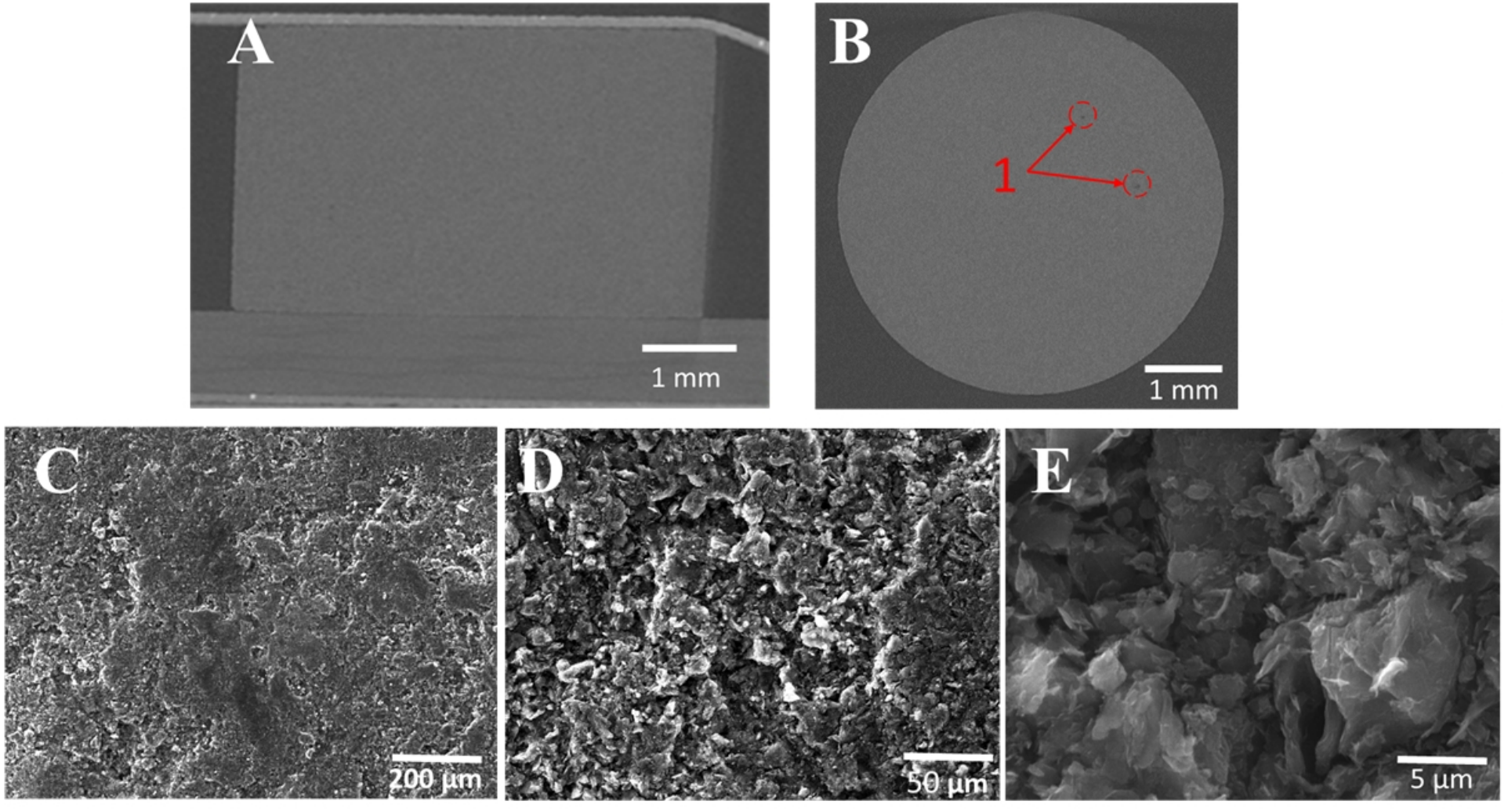
A
1 mm
B
1
1 mm
C
200 µm
D
50 µm
E
5 µm

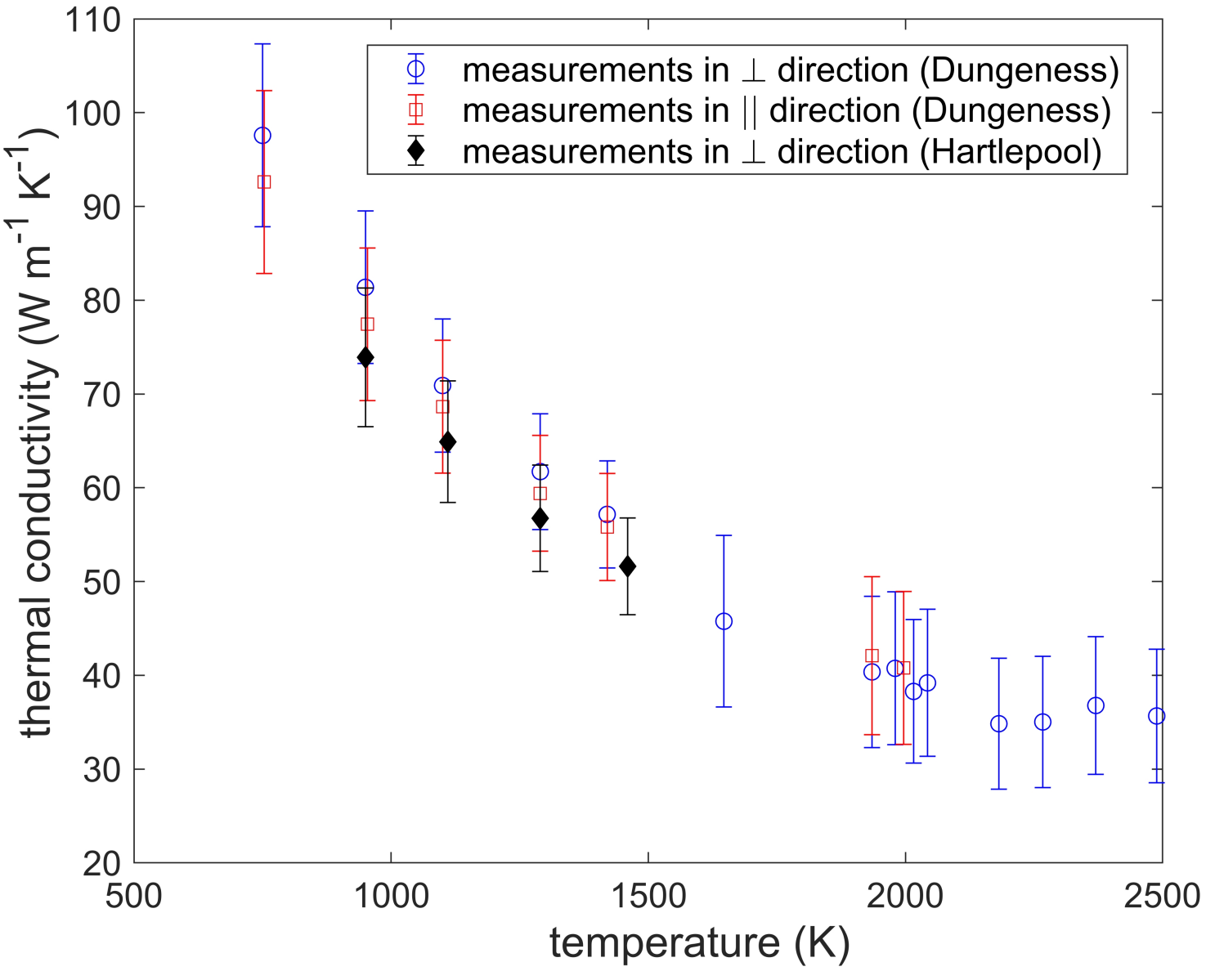
measurements in ⊥ direction (Dungeness)
measurements in || direction (Dungeness)
measurements in ⊥ direction (Hartlepool)
thermal conductivity (W m-1 K-1)
temperature (K)
110
100
90
80
70
60
50
40
30
20
500
1000
1500
2000
2500